



**HAL**  
open science

# Coupling between topology optimization and digital image correlation for the design of specimen dedicated to selected material parameters identification

Ludovic Chamoin, Clément Jailin, Matthieu Diaz, Lucas Quesada

## ► To cite this version:

Ludovic Chamoin, Clément Jailin, Matthieu Diaz, Lucas Quesada. Coupling between topology optimization and digital image correlation for the design of specimen dedicated to selected material parameters identification. *International Journal of Solids and Structures*, 2020, 193-194, pp.270-286. 10.1016/j.ijsolstr.2020.02.032 . hal-02484421

**HAL Id: hal-02484421**

**<https://hal.science/hal-02484421>**

Submitted on 7 Mar 2022

**HAL** is a multi-disciplinary open access archive for the deposit and dissemination of scientific research documents, whether they are published or not. The documents may come from teaching and research institutions in France or abroad, or from public or private research centers.

L'archive ouverte pluridisciplinaire **HAL**, est destinée au dépôt et à la diffusion de documents scientifiques de niveau recherche, publiés ou non, émanant des établissements d'enseignement et de recherche français ou étrangers, des laboratoires publics ou privés.



Distributed under a Creative Commons Attribution - NonCommercial 4.0 International License

# Coupling between topology optimization and digital image correlation for the design of specimen dedicated to selected material parameters identification

L. Chamoin<sup>a,b,\*</sup>, C. Jailin<sup>a</sup>, M. Diaz<sup>c</sup>, L. Quesada<sup>c</sup>

<sup>a</sup>*Université Paris-Saclay, ENS Paris-Saclay, CNRS, LMT - Laboratoire de Mécanique et Technologie  
61 avenue du Président Wilson, 94235 Cachan, France*

<sup>b</sup>*Institut Universitaire de France (IUF)  
1 rue Descartes, 75231 Paris Cedex 05, France*

<sup>c</sup>*Université Paris-Saclay, ENS Paris-Saclay, Department of Mechanical Engineering  
61 avenue du Président Wilson, 94235 Cachan, France*

---

## Abstract

The work addresses the optimization of specimen geometry in the context of parameter identification from full-field measurements. For this purpose, we propose to use topology optimization tools in order to maximize the sensitivity of the measured displacement field to sought parameters, under volume fraction constraints and without any a priori information on the specimen shape. The associated cost function is conveniently defined from sensitivity fields which are directly available from the identification procedure. In addition, further analyzes are conducted in order to fully set the theoretical and numerical aspects of the methodology, and enhance both stability and convergence properties. Numerical experiments illustrate the interest of the proposed approach, while its validation is performed from a real identification test using a specimen with optimized topology.

*Keywords:* Topology optimization, Parameter identification, Digital Image Correlation, Sensitivity analysis

---

---

\*. Corresponding author

*Email addresses:* ludovic.chamoin@ens-paris-saclay.fr (L. Chamoin),  
clement.jailin@ens-paris-saclay.fr (C. Jailin), mathieu.diaz@ens-paris-saclay.fr (M. Diaz),  
lucas.quesada@ens-paris-saclay.fr (L. Quesada)

*Preprint submitted to International Journal of Solids and Structures*

*17 février 2020*

## 1. Introduction

Parameter identification methods have become increasingly sophisticated and powerful in solid mechanics in order to qualify material behaviors at best and feed numerical simulations. Among the large scope of inverse identification methods, we focus here on those based on full-field measurements, i.e. performed from digital image correlation (DIC) using a single camera [34, 36], stereo image correlation (stereo-DIC) using several cameras [30], or digital volume correlation (DVC) using X-ray microtomography or magnetic resonance imaging (MRI) [10]. Overviews of available identification techniques from such measurements can be found in [9, 33]. The exploitation of full-field measurements, initiated more than 30 years ago [40, 69] but widely studied and applied during the last two decades [42, 63, 61, 47, 38], constitutes a main breakthrough in the fields of material science and computational mechanics [8, 70, 51]. It allows in particular to set up heterogeneous mechanical tests, with numerous (but noisy) measurement information, in order to identify parameters of complex constitutive models such as those used for composites [24, 11, 19, 31]. For instance, nowadays experiments on simple flat samples use, typically, 1000 16-bit images with up to 100-Mpixel definition for the measurement of 2D displacement fields, which provides for 2-200 Gbyte data sets. This is in opposition with classical tests in which homogeneity is assumed. However, due to the large and eclectic amount of experimental data that may be obtained from full-field measurements (compared with classical measurement devices such as extensometers or strain gauges), an important and actual challenge is to extract from these data the part of information which is relevant for the identification objective [51]. In order to do so, one way consists in a filtering process when post-processing the large amount of data coming from DIC, so that only a small part of relevant data is conserved. Another option consists in devising the experimental protocol (specimen geometry, loading conditions and history) so that a limited amount of measured data constitutes very rich information for the identification purpose. In this latter framework, it is of interest to design optimal specimen on which to perform full-field measurements, maximizing the sensitivity of the obtained displacement field with respect to the sought parameters and therefore obtain an effective identification

29 procedure. This is the topic of the present work. We point out here that such a design of  
30 optimal specimen to be tested can not be performed for all material identification problems  
31 encountered in real-life applications. It can be conducted in practice for some specific ap-  
32 plications of interest allowing a sufficient flexibility on the specimen geometry, such as the  
33 identification of constitutive parameters and laws by means of research lab facilities ; this is  
34 the targeted application in the remainder of the paper.

35

36 Until now, very few research works addressed the definition of specific specimen geome-  
37 try for identification from full-field measurements. These consider sub-optimal approaches  
38 in which the specimen shape is constrained *a priori*, i.e. the specimen topology is given,  
39 leading to a small number of design parameters to set. For instance, shape optimization in  
40 the context of DIC-FEMU or integrated DIC (IDIC) for parametrized specimen was recently  
41 carried out in [15, 50] considering the Poisson ratio identification with plates under biaxial  
42 traction, and with a small amount of design variables related to curvature radii. We also refer  
43 to [49, 28] for the design of heterogeneous tests adding holes to different samples shapes,  
44 to [45] for the design of cruciform sample geometries operated with bi-axial tensile devices,  
45 to [56] for the full design (loading and specimen geometry) of an original test in the context  
46 of stereo image correlation, enabling to identify several parameters of an anisotropic plastic  
47 constitutive model from only one test, or to [39] for the comparison of sensitivities to an  
48 internal length for a damage model from two different tests.

49 In the present work we wish to go one step further by using topology optimization [13, 65,  
50 1, 14] and associated iterative optimization procedures in order to automatically define the  
51 spatial material distribution inside the working space (for given loading conditions and vo-  
52 lume fraction), so that a further optimized specimen shape is obtained without any *a priori*  
53 information on the topology. Consequently, the heterogeneity of the identification test is in  
54 this case fully induced by the definition of an original and optimized specimen geometry.  
55 This is, to the best of the authors knowledge, the first attempt to use topology optimization  
56 in conjunction with full-field measurements. We consider here two-dimensional problems ;  
57 the full-field measurements are obtained from DIC, and the identification procedure is per-

58 formed using the FEMU approach. The goal is thus to couple the DIC-FEMU technology  
59 with topology optimization, leading to the definition of specific specimen in which the mea-  
60 sured displacement field would be highly sensitive to the constitutive parameters of interest.  
61 Regarding the topology optimization procedure, we consider here the SIMP (Solid Isotropic  
62 Material with Penalization) approach, and we use the constrained optimization algorithm  
63 implemented in the `top99.m` Matlab code developed in [65]. The core of the research work  
64 consists in the definition of a convenient cost function based on sensitivity fields which may  
65 be recovered in a straightforward manner from Hessian matrices in DIC-FEMU. Additio-  
66 nal ingredients are then introduced in the cost function in order to enhance stability and  
67 convergence properties of the optimization procedure. Several issues, such as the setting of  
68 initial conditions or multi-parameter optimization, are also addressed. The performance of  
69 the approach is illustrated on several numerical examples, and an experimental validation  
70 of the optimized specimen is also shown.

71

72 The remainder of the paper is organized as follows : in Section 2, basic aspects of DIC  
73 and FEMU methods for parameter identification from full-field measurements are recalled ;  
74 the coupling between DIC-FEMU and topology optimization, which is the main contribu-  
75 tion of the paper, is addressed in Section 3 ; several numerical experiments, as well as an  
76 experimental validation, are reported in Section 4 ; eventually, conclusions and prospects are  
77 drawn in Section 5.

## 78 **2. Basics on DIC and FEMU methods**

### 79 *2.1. The DIC method for full-field measurement*

80 Digital image correlation (DIC) is a powerful technique used in solid mechanics to provide  
81 full-field displacement measurements from mechanical tests of materials and structures [69,  
82 34, 36]. It consists in registering two (or more) images of the same scene, that are large  
83 sets of pixels with distribution of gray level values (encoded over few bits, typically 8 to  
84 16, and stored as matrices), and extracting displacement fields that enable the best match

85 between the image frames. In practice, gray levels are given by a speckle applied to the  
 86 target zone which provides irregular picture texture. In the following, we consider only two  
 87 images : a reference image  $f(\mathbf{x})$  and a deformed image  $g(\mathbf{x})$ ;  $\mathbf{x}$  denotes the discrete, and thus  
 88 discontinuous, pixel (or voxel in 3D) position, while  $f$  and  $g$  refer to gray level magnitudes.  
 89 In this framework, approaches to recover a measured displacement field  $\mathbf{u}(\mathbf{x})$  from the two  
 90 image frames are based on the local gray level conservation  $f(\mathbf{x}) = g(\mathbf{x} + \mathbf{u}(\mathbf{x}))$ . Considering  
 91 a first-order Taylor expansion (small perturbations regime) and gradients at theoretical  
 92 convergence (so that  $\nabla g$  can be approximated with  $\nabla f$ ), this conservation can also be  
 93 written as (see [36]) :

$$f(\mathbf{x}) - g(\mathbf{x}) - \nabla f \cdot \mathbf{u}(\mathbf{x}) = 0 \quad (1)$$

94 or using an iterative sequential construction of  $\mathbf{u}$  :

$$f(\mathbf{x}) - \tilde{g}(\mathbf{x}) - \nabla f \cdot \delta\mathbf{u}^{(k)}(\mathbf{x}) = 0 \quad (2)$$

95 with  $\tilde{g}(\mathbf{x}) = g(\mathbf{x} + \mathbf{u}^{(k)}(\mathbf{x}))$  the updated deformed image, and  $\delta\mathbf{u}^{(k)} = \mathbf{u}^{(k+1)} - \mathbf{u}^{(k)}$  the  
 96 correction at iteration  $k$ .

97 In all practical cases, the local gray level conservation is not strictly satisfied due to  
 98 noise, so that regularization is required. A suitable norm  $\|f - g(\cdot + \mathbf{u})\|$  between the signal  
 99 difference (gray level residual) is then chosen with respect to the noise [21] and minimized  
 100 with respect to  $\mathbf{u}$ . The usual choice of the  $L^2$ -norm (mean quadratic gap) provides the  
 101 correlation residual functional. Approaches for the computation of  $\mathbf{u}(\mathbf{x})$  can then be split  
 102 in two categories, depending on the domains on which the gray level residual is defined and  
 103 the way the underlying ill-posed problem is regularized :

- 104 • local DIC approaches (widely employed in commercial DIC codes) use a local mat-  
 105 ching procedure on sub-images or zones of interest (ZOI), treated independently. The  
 106 norm then reads :

$$\sum_{\mathbf{x} \in \text{ZOI}} (f(\mathbf{x}) - g(\mathbf{x} + \mathbf{u}(\mathbf{x})))^2 \quad (3)$$

107 When  $\mathbf{u}$  is chosen constant locally, the minimization of (3) is equivalent to maximizing  
 108 the cross-correlation  $(f * g)(\mathbf{u}) = \sum_{\mathbf{x} \in \text{ZOI}} f(\mathbf{x})g(\mathbf{x} + \mathbf{u})$ . Classically, linear or quadratic

109 displacement fields are used for each ZOI, but the only output of the analysis is still  
 110 the mean displacement at the middle of the ZOI. In local approaches, the small size  
 111 of the ZOI naturally introduces a filtering of the displacement field and drives the  
 112 measurement uncertainties ;

113 • global DIC approaches use a norm defined over the whole measurement zone (region of  
 114 interest or ROI), containing a large number  $N_p$  of pixels, so that a global (nonlinear)  
 115 correlation residual is minimized :

$$\frac{1}{N_p} \sum_{\mathbf{x} \in ROI} (f(\mathbf{x}) - g(\mathbf{x} + \mathbf{u}(\mathbf{x})))^2 \quad (4)$$

116 This leads to a variational formulation with successive linearizations (using (2))  
 117 and corrections (iterative Newton-Raphson scheme) in which a new picture  $\tilde{g}(\mathbf{x}) =$   
 118  $g(\mathbf{x} + \mathbf{u}^{(k)}(\mathbf{x}))$  is constructed at each iteration using the current estimate  $\mathbf{u}^{(k)}$  at ite-  
 119 ration  $k$  and (spline) gray level interpolations when sub-pixel resolutions are sought.  
 120 As the minimization of (4) is ill-posed and can not be solved as such (the displa-  
 121 cement is only detectable along the direction of  $\nabla f$ ), these last approaches require  
 122 regularization such as Tikhonov regularization on gradients associated with  $\mathbf{u}$  (glo-  
 123 bal constraint of smoothness), regularization from the balance equations (equilibrium  
 124 residual gap) [60], or regularization via the choice of a finite-dimensional kinematic  
 125 subspace (decomposing  $\mathbf{u}$  on a meaningful basis).

126 **Remark 1.** Pixels being poor sensors, the covariance matrix  $\mathbb{C}_n = [C_n(\mathbf{x}, \boldsymbol{\xi})]$  of gray level  
 127 noise for pixels  $\mathbf{x}$  and  $\boldsymbol{\xi}$  can be introduced in the global correlation residual. It leads to the  
 128 minimization of the Mahalanobis distance between the two images :

$$\frac{1}{N_p} \sum_{\mathbf{x} \in ROI} \sum_{\boldsymbol{\xi} \in ROI} (f(\mathbf{x}) - g(\mathbf{x} + \mathbf{u}(\mathbf{x}))) [C_n(\mathbf{x}, \boldsymbol{\xi})]^{-1} (f(\boldsymbol{\xi}) - g(\boldsymbol{\xi} + \mathbf{u}(\boldsymbol{\xi}))) \quad (5)$$

129 which is optimal and refers to the maximum likelihood with Gaussian distributions [64]. As-  
 130 suming white Gaussian (i.e. spatially uncorrelated) acquisition noise induces that  $[C_n(\mathbf{x}, \boldsymbol{\xi})] =$   
 131  $\gamma_f^2 [\delta(\mathbf{x}, \boldsymbol{\xi})]$  or  $\mathbb{C}_n = \gamma_f^2 \mathbb{I}$  where  $\gamma_f$  is the standard deviation of noise, so that the functional

132 reads

$$\frac{1}{2\gamma_f^2 N_p} \sum_{\mathbf{x} \in ROI} (f(\mathbf{x}) - g(\mathbf{x} + \mathbf{u}(\mathbf{x})))^2 \quad (6)$$

133 Noise is assumed to affect each image  $f$  and  $g$  independently, which is responsible for the  
 134 factor  $1/2$  coming as a multiplicative term in the functional. This is equivalent to reporting  
 135 the noise on the deformed image  $g$  only and to increase it by a factor 2.

136 In the following, we consider global DIC with regularization based on a finite element  
 137 kinematic basis; this approach is referred to as FE-DIC. We thus write  $\mathbf{u} = \mathbb{N}\mathbf{U}$ , with  $\mathbb{N}$   
 138 gathering the FEM basis functions and  $\mathbf{U}$  denoting the vector of unknown nodal values.  
 139 The linear system associated with the minimization, at each iteration  $k$ , of the quadratic  
 140 functional issued from (2) and (4) thus reads :

$$\mathbb{M}_{DIC} \delta \mathbf{U}^{(k)} = \mathbf{b}_{DIC}^{(k)} \quad (7)$$

141 with

$$\begin{aligned} \mathbb{M}_{DIC} &= \sum_{\mathbf{x} \in ROI} \mathbb{N}^T \{ \nabla f \} \{ \nabla f \}^T \mathbb{N} \quad (\text{symmetric positive DIC matrix, computed once for all}) \\ \mathbf{b}_{DIC}^{(k)} &= \sum_{\mathbf{x} \in ROI} (f - \tilde{g}) \mathbb{N}^T \{ \nabla f \} \quad (\text{residual vector updated at iteration } k) \end{aligned} \quad (8)$$

142 In the general case, the matrix  $\mathbb{M}_{DIC}$  is positive semi-definite. If the image contrast is  
 143 sufficiently fine-scaled with respect to the element size, then  $\mathbb{M}_{DIC}$  may be positive definite  
 144 and hence the problem is solvable. This condition also implies that the mesh cannot be  
 145 arbitrarily fine, as along with fineness comes first ill-conditioning, and second ill-posedness  
 146 (i.e. rank-deficient Hessian) as for the pixel-wise case.

147 Furthermore, and even though it enables to better capture complex geometries and dis-  
 148 placement fluctuations, increasing the spatial resolution with finer FE mesh also increases  
 149 uncertainty (as fewer pixels are then available to determine the value of the kinematic dofs).  
 150 An explicit characterization of the effect of image noise on displacement uncertainty can be  
 151 introduced by evaluating the covariance matrix  $\mathbb{C}_U$  of the measured dofs. From (7), it is

152 straightforward (see [16, 62, 37]) that :

$$\langle \delta \mathbf{U} \rangle = 0 \quad (\text{no systematic bias}) \quad ; \quad \mathbb{C}_U = \langle \delta \mathbf{U} \cdot \delta \mathbf{U}^T \rangle = 2\gamma_f^2 \mathbb{M}_{DIC}^{-1} \quad (9)$$

153 which shows that the displacement noise is spatially correlated ( $\mathbb{M}_{DIC}^{-1}$  is not diagonal), and  
 154 that zones with low contrast (such as small FE elements with few pixels per element) are  
 155 particularly subjected to measurement uncertainties. Also, the measured displacement on  
 156 nodes located on the boundary of the ROI are more sensitive to noise due to their reduced  
 157 connectivity. Alternative approaches have been recently developed to overcome the tricky  
 158 compromise between spatial resolution and uncertainty, such as multiscale approaches [54]  
 159 or integrated methods (see Section 2.2.2).

160 **Remark 2.** The correlation residual field provides a good indication on the quality of the  
 161 obtained displacement  $\mathbf{u}$ . It is ideally expected to consist of white noise, with a dimensionless  
 162 variance of 1. Otherwise, correlation residuals may be used to locally enrich the kinematic  
 163 basis (refining the mesh or adding richer basis functions such as those used in XFEM to  
 164 describe discontinuities [59]).

165 In brief, the outputs of DIC analysis are therefore a displacement field  $\mathbf{U}$  over a kinematic  
 166 basis, as well as the correlation residuals map and noise sensitivity (via the covariance matrix  
 167  $\mathbb{C}_U$ ) which enable to adjust DIC parameters and to weigh the measured information as  
 168 it should. These quantities constitute the inputs of the identification procedure described  
 169 below.

## 170 *2.2. FEMU and I-DIC methods for identification from full-field measurements*

### 171 *2.2.1. The FEMU method*

172 The measured displacement field, denoted  $\mathbf{u}_m = \mathbb{N}\mathbf{U}_m$  and previously obtained from  
 173 global DIC, can be used for indirect identification of a model parameter vector  $\mathbf{p}$ , each  
 174 component of  $\mathbf{p}$  being conveniently designed to be dimensionless (e.g. normalization with  
 175 nominal values of the parameters). Among all possible identification methods available with

176 full-field measurements (see [9] for an overview), FEMU is probably the most popular one.  
 177 In its FEMU-U version, it is an incremental method that aims at minimizing the gap bet-  
 178 ween a simulated displacement field  $\mathbf{u}_s$  (obtained from a FE computation with constitutive  
 179 model parametrized by  $\mathbf{p}$  and boundary conditions extracted from DIC) and the measured  
 180 displacement field  $\mathbf{u}_m$ . It thus consists in an iterative correction of a FE solution from mea-  
 181 surements, by varying the parameter set  $\mathbf{p}$  to be identified, and usually considering the same  
 182 mesh to represent  $\mathbf{u}_m$  and  $\mathbf{u}_s$ .

183 Denoting by  $N_U$  the total number of kinematic dofs, the following cost function is introdu-  
 184 ced :

$$\mathcal{T}_U(\mathbf{p}) = \frac{1}{N_U} [\mathbf{U}_s(\mathbf{p}) - \mathbf{U}_m]^T \mathbb{C}_U^{-1} [\mathbf{U}_s(\mathbf{p}) - \mathbf{U}_m] \quad (10)$$

185 It uses an appropriate metric defined from the covariance matrix  $\mathbb{C}_U$ , which provides optimal  
 186 robustness as it naturally propagates the impact of noise coming from images onto the  
 187 uncertainty of the identified parameters [47]. An approximation of  $\mathbb{C}_U$  by means of a mass  
 188 matrix (mean field assumption) may be sufficient and preferred in the definition of  $\mathcal{T}_U(\mathbf{p})$ .  
 189 Furthermore, the prefactor  $1/N_U$  is chosen so that, at convergence, noise in the measured  
 190 displacement should by itself endow  $\mathcal{T}_U(\mathbf{p}) = 1$ .

191 The minimization of  $\mathcal{T}_U(\mathbf{p})$  can be conducted in an iterative way from a Gauss-Newton  
 192 gradient descent. For that purpose, a first-order Taylor expansion is introduced :

$$\mathbf{U}_s(\mathbf{p}^{(n)} + \delta\mathbf{p}^{(n)}) = \mathbf{U}_s(\mathbf{p}^{(n)}) + \mathbb{S}_{\mathbf{p}} \delta\mathbf{p}^{(n)} \quad (11)$$

193 where  $\delta\mathbf{p}^{(n)}$  is the infinitesimal correction of  $\mathbf{p}$  at iteration  $n$ , and  $\mathbb{S}_{\mathbf{p}} = \partial\mathbf{U}_s/\partial\mathbf{p}$  is the matrix  
 194 of sensitivity fields (quantitative measurement of the sensitivity of the displacement field to  
 195 the studied parameters) expressed in pixels. A Newton-Raphson scheme then provides for  
 196 the following linear system at iteration  $n$  :

$$\mathbb{H}_{FEMU} \delta\mathbf{p}^{(n)} = \mathbf{b}_{FEMU}^{(n)} \quad (12)$$

197 with

$$\mathbb{H}_{FEMU} = \mathbb{S}_{\mathbf{p}}^T \mathbb{C}_U^{-1} \mathbb{S}_{\mathbf{p}} = \frac{1}{2\gamma_f^2} \mathbb{S}_{\mathbf{p}}^T \mathbb{M}_{DIC} \mathbb{S}_{\mathbf{p}} \quad (\text{Hessian matrix}) \quad (13)$$

$$\mathbf{b}_{FEMU}^{(n)} = \mathbb{S}_{\mathbf{p}}^T \mathbb{C}_U^{-1} (\mathbf{U}_m - \mathbf{U}_s(\mathbf{p}^{(n)}))$$

198 The matrix  $\mathbb{H}_{FEMU}$ , which is the restriction of  $\mathbb{M}_{DIC}$  to the subspace generated by sensitivity  
 199 fields, is smaller sized and better conditioned than  $\mathbb{M}_{DIC}$ . When the original system (12)  
 200 remains badly conditioned, the Levenberg-Marquardt algorithm [46] with enhanced stability  
 201 properties should be preferred to the Gauss-Newton one.

202

203 At convergence, the fluctuating part  $\delta\mathbf{p}$  of the identified parameters due to noise is  
 204  $\delta\mathbf{p} = \mathbb{H}_{FEMU}^{-1} \mathbb{S}_{\mathbf{p}}^T \mathbb{C}_U^{-1} (\mathbf{U}_m - \mathbf{U}_s(\mathbf{p}))$ . The global covariance matrix of the identified parameters  
 205 due to image noise thus reads :

$$\mathbb{C}_{\mathbf{p}} = \langle \delta\mathbf{p} \cdot \delta\mathbf{p}^T \rangle = \mathbb{H}_{FEMU}^{-1} \quad (14)$$

206 It enables to track down the uncertainties from the measurement step (pixel level) down  
 207 to the identification step (parameter level). Accurate identification resulting from the good  
 208 conditioning of the positive symmetric matrix  $\mathbb{H}_{FEMU}$ , several scalar criteria qualifying the  
 209 robustness of multi-parameter identification can then be defined, such as : (i) maximizing  
 210 the smallest eigenvalue of  $\mathbb{H}_{FEMU}$  (worst case) so that all parameters are determined accura-  
 211 tely [15]; (ii) maximizing the ratio between the smallest and the largest eigenvalues [28]; (iii)  
 212 considering the uncertainty volume  $\det(\mathbb{H}_{FEMU})$ . We will refer to this point in Section 3.2.

213 **Remark 3.** Reaction forces may also be measured and compared with computed resultants.  
 214 Thus, an additional term can be added in the FEMU functional to minimize [15]. It is of  
 215 the form :

$$\mathcal{T}_F(\mathbf{p}) = \frac{1}{N_F} \{ \mathbf{F}_s(\mathbf{p}) - \mathbf{F}_m \}^T \mathbb{C}_{F_m}^{-1} \{ \mathbf{F}_s(\mathbf{p}) - \mathbf{F}_m \} \quad (15)$$

216 where  $N_F$  is the number of load cells,  $\mathbf{F}_m$  the measured forces,  $\mathbf{F}_s$  the computed reaction  
 217 forces with respect to the parameter set  $\mathbf{p}$ , and  $\mathbb{C}_{F_m}$  the covariance matrix of the measured  
 218 loads. The identification based on the combined displacement fields and reaction forces is  
 219 then achieved by minimizing the global functional :

$$\mathcal{T}_{UF}(\mathbf{p}) = \frac{N_U}{N_U + N_F} \mathcal{T}_U(\mathbf{p}) + \frac{N_F}{N_U + N_F} \mathcal{T}_F(\mathbf{p}) \quad (16)$$

220 *2.2.2. Integrated approach : I-DIC*

221 In the previously described two-step DIC-FEMU procedure, displacement data are only  
 222 an intermediate quantity whose computation may imply constraints that are not ideal to  
 223 FEMU. The idea in integrated DIC (I-DIC) is to merge measurement and identification  
 224 procedures in a single step by using directly the images (rather than a measured displacement  
 225 field) to determine material parameters. This allows standard FE codes to be used in a non-  
 226 intrusive way. In the I-DIC framework, the gap between image frames  $f$  and  $g$  is minimized  
 227 using a specific kinematics driven by a parametrized model (strong mechanical content),  
 228 rather than simple standard FE representations. Dofs in DIC are therefore directly related  
 229 to the parameters to be identified (elasticity parameters, stress intensity factors, ...). The  
 230 functional to be minimized reads :

$$\frac{1}{2\gamma_f^2|\Omega|} \sum_{\mathbf{x} \in ROI} (f(\mathbf{x}) - g(\mathbf{x} + \mathbf{u}(\mathbf{x}, \mathbf{p})))^2 \quad (17)$$

231 It leads to the solution of linear systems of the form (at iteration  $n$ ) :

$$\mathbb{H}_{IDIC} \delta \mathbf{p}^{(n)} = \mathbf{b}_{IDIC}^{(n)} \quad (18)$$

232 with

$$\mathbb{H}_{IDIC} = \mathbb{S}_{\mathbf{p}}^T \mathbb{M}_{DIC} \mathbb{S}_{\mathbf{p}} \quad (\text{Hessian matrix}) \quad ; \quad \mathbf{b}_{IDIC}^{(n)} = \mathbb{S}_{\mathbf{p}}^T \mathbf{b}_{DIC}^{(n)} \quad (19)$$

233 which indicates that I-DIC merely consists in projecting the nodal displacement field onto  
 234 the sensitivity fields. In practice, the I-DIC procedure uses closed-form solutions which can  
 235 be obtained analytically, from FEM, or from ROM (parametrized solutions). This may en-  
 236 able to assess sensitivity fields very efficiently [43].

237  
 238 In theory, if the same mesh is used in DIC and for the computation of sensitivity fields,  
 239 the two-step DIC-FEMU procedure and the integrated I-DIC procedure (in which the DIC  
 240 mesh has disappeared) should be equivalent. However, this is valid only for small amplitudes  
 241 of noise, appropriate metric (weighting) in FEMU, and when the smallest element size is not  
 242 critical for DIC. A fine mesh size is not a problem in I-DIC as only a few search directions

243 are chosen (i.e. dofs are not nodal displacements but unknown material parameters), so  
244 that the modeling error due to a coarse mesh can be avoided. Consequently, as long as the  
245 approximation error due to the mesh remains well below the uncertainty of DIC, a coarse  
246 mesh is beneficial, but a finer mesh can also be used with I-DIC if required (depending on  
247 the complexity of the sample geometry complexity or the picture contrast). In [43], it was  
248 proposed to choose the element size of the mesh in I-DIC as a decreasing function of the  
249 sensitivity to the studied parameters.

250 **Remark 4.** In I-DIC, correlation residuals with appropriate normalization can be conve-  
251 niently used to assess the relevance of the mechanical model for explaining the observations.  
252 They can indeed be used to measure the quality of the identification and guide toward suc-  
253 cessive enrichment of the constitutive model to progressively reduce the experiment-model  
254 gap [50].

255 In the next section, we design specimen geometries which maximize the sensitivity (and  
256 therefore minimize uncertainty) in the parameter identification step. This is performed using  
257 topology optimization associated to a suitable cost function based on eigenvalues of Hessian  
258 matrices  $\mathbb{H}_{FEMU}$  or  $\mathbb{H}_{IDIC}$ . As an illustration, we plot in Fig. 1 the numerical sensitivity fields  
259 with respect to the shear modulus  $G_{12}$  for three specimen (with different shapes) made of an  
260 orthotropic linear elastic material (with plane stress assumption, and uniformly distributed  
261 orthotropy direction) submitted to a pure traction loading with prescribed longitudinal  
262 displacement on the right side. On the one hand, and as expected, the first specimen with  
263 rectangular shape does not provide any piece of information for the identification of the  
264 parameter  $G_{12}$ . On the other hand, the second specimen (rectangular shape with hole in  
265 the center) and third specimen (with unconventional geometry) generate an heterogeneous  
266 displacement field that makes it sensitive to  $G_{12}$ . The geometry of the third specimen, in  
267 which sensitivity is the largest, has been designed using the topology optimization tools  
268 which are developed in this work. It leads to a gain of about  $10^3$  in the sensitivity compared  
269 to the specimen with a hole and with similar volume fraction.

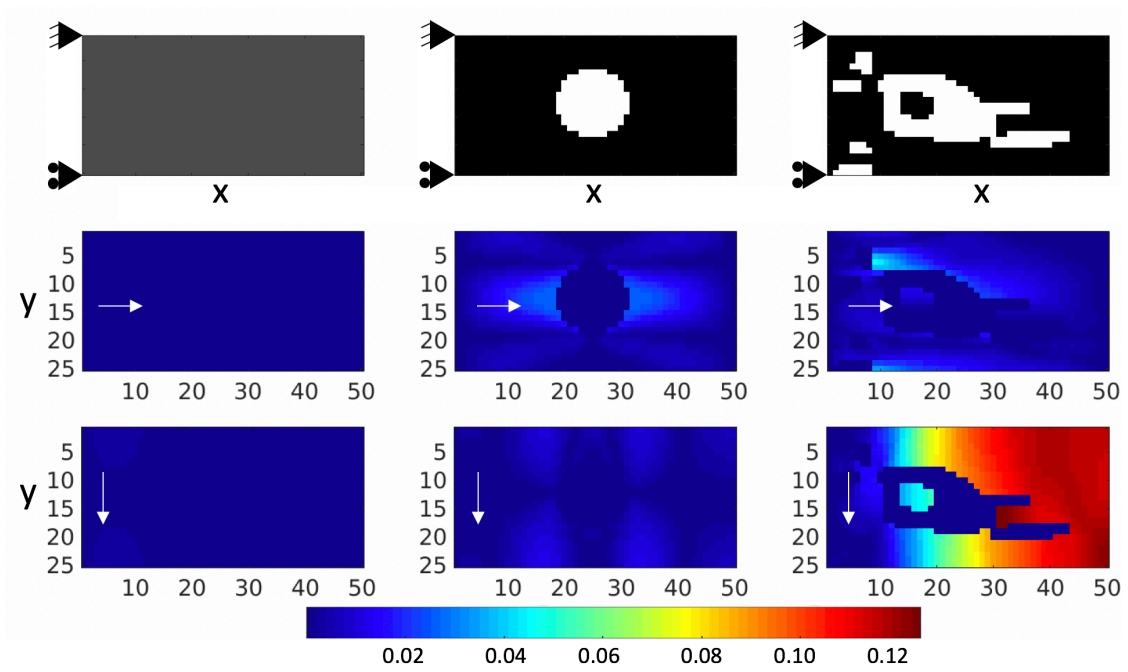


FIGURE 1: Comparison of sensitivity fields for three different specimen (from left to right) under traction loading, with geometry,  $x$  component and  $y$  component of the sensitivity field (from top to bottom).

### 270 **3. Coupling between DIC-FEMU and topology optimization**

#### 271 *3.1. Background on topology optimization*

##### 272 *3.1.1. General framework*

273 Topology optimization, initiated in [12], is a well-known method for weight reductions  
274 of structures, which is a crucial issue in many structural engineering applications. It is also  
275 a tool of choice for the design of meta-materials by a suitable arrangement of the micro-  
276 structure [41, 23]. Basically, it is a mathematical process which consists in the automatic  
277 optimization of the material distribution in a given volume, under specific constraints and  
278 with respect to given optimality criteria (objective function). In practice, most applications  
279 consider structural stiffness as the cost function (minimization of the structural compliance),  
280 and constraints deal with volume fraction (total mass) in addition to solving the mechanical  
281 problem of interest with given loadings [65, 57]. When considering structures with isotropic  
282 materials, methodologies for topology optimization are abundant in the literature; survey  
283 developments can be found in [66]. Two main approaches have been investigated so far :  
284 density-based methods and boundary variation methods. The first group of methods uses a  
285 local density variable to define if there should be solid material (variable set to 1) or void  
286 (variable set to 0) in subdomains of the structure. The discrete problem associated to den-  
287 sity variables is usually turned into a continuous one, leading to intermediate densities that  
288 may be difficult to interpret. Several penalization methods can then be used to steer the  
289 solution toward a discrete solid/void solution, among which SIMP (Solid Isotropic Material  
290 Penalization) [13], RAMP (Rational Approximation of Material Properties) [68], SINH [20],  
291 or SRV (using reciprocal variables) [29]. In the second group of methods, we refer to the level  
292 set method [2, 22] that uses a scalar function to represent the boundaries, and the phase  
293 field method [18] that uses a phase field function over a domain composed of two phases.  
294 Compared with density-based methods, boundary variation methods provide a clear contour  
295 of the shape and an explicit definition of geometrical parameters. They do not require a pe-  
296 nalization method, but the computation of topological gradients and the construction of  
297 complex interpolation schemes are necessary [52].

298 In the present work, a density-based method is used and the SIMP method is employed as a  
 299 penalization method. This latter method has been applied to a broad range of applications  
 300 and physical models [41, 72, 25, 32, 27, 26, 23] and is nowadays implemented in various  
 301 commercial tools in the field of mechanics and multiphysics.

### 302 3.1.2. Practical implementation

303 In the SIMP method framework, we consider the methodology developed in [65, 7] for the  
 304 structural stiffness maximization with two-dimensional applications and with plane stress  
 305 assumption. The working space is divided in subdomains or elements  $e$  (usually defined from  
 306 a regular mesh with Q4 elements), and the topology of the structure is parameterized by a  
 307 set of density variables  $\rho_e \in [\rho_{min}, 1]$ , with  $\rho_{min} > 0$  (to keep the mechanical problem well-  
 308 posed) that determines the presence or absence of material in each individual element  $e$ . A  
 309 global structural stiffness maximization problem written as a compliance (or complementary  
 310 energy) minimization problem is then treated, and a volume constraint is applied.

311 Using the FE framework with a regular mesh made of  $N_e$  elements, and denoting by  
 312  $\boldsymbol{\rho} = \{\rho_e\}$  the set of density variables, the cost function to be minimized reads :

$$c(\boldsymbol{\rho}) = \mathbf{U}^T(\boldsymbol{\rho})\mathbb{K}(\boldsymbol{\rho})\mathbf{U}(\boldsymbol{\rho}) = \sum_{e=1}^{N_e} \rho_e^\gamma \mathbf{U}_e^T \mathbb{K}_0 \mathbf{U}_e \quad (20)$$

313  $\mathbf{U}(\boldsymbol{\rho})$  is the vector of nodal displacements, solution of the mechanical FE problem  $\mathbb{K}(\boldsymbol{\rho})\mathbf{U}(\boldsymbol{\rho}) =$   
 314  $\mathbf{F}$ , and  $\mathbb{K}_0$  is the elementary stiffness matrix (with full material density). The penalty factor  
 315  $\gamma$  weighs the impact of material density changes in the stiffness, so that it enables to mo-  
 316 dulate the black and white contrast in the optimized structure as well as the convergence  
 317 speed of the optimization algorithm.

318 **Remark 5.** In the previous context, gradients  $\partial c / \partial \rho_e$  can be computed analytically, and it  
 319 is easy to show that :

$$\frac{\partial c}{\partial \rho_e} = -\gamma \rho_e^{\gamma-1} \mathbf{U}_e^T \mathbb{K}_0 \mathbf{U}_e \quad (21)$$

320 Introducing the targeted volume fraction  $f_v$ , the associated constraint reads  $V(\boldsymbol{\rho}) = f_v V_0$

321 with  $V_0$  the total volume of the working space and  $V(\boldsymbol{\rho}) = \frac{V_0}{N_e} \sum_{e=1}^{N_e} \rho_e$  the actual material  
 322 volume. The optimization procedure thus leads to a constrained minimization which is ad-  
 323 dressed using the following Lagrangian functional with scalar Lagrange multiplier  $\lambda$  :

$$\mathcal{L}(\boldsymbol{\rho}, \lambda) = c(\boldsymbol{\rho}) + \lambda(V(\boldsymbol{\rho}) - f_v V_0) \quad (22)$$

324 The search of the saddle point of  $\mathcal{L}$  leads to the solution of constrained minimization pro-  
 325 blems. In practice, this search can be performed using various techniques dedicated to non-  
 326 linear constrained minimizations. Among them, we mention the Sequential Linear Program-  
 327 ming (SLP) performing sequential first order approximations [53], or the Methods of Mo-  
 328 ving Asymptotes (MMA) [71]. Here, and as performed in [65], we use the optimality criteria  
 329 method which is suited for the optimization of a simple energy functional with a single  
 330 constraint. This is an iterative technique which defines an updated approximation  $\lambda^{(k)}$  of  
 331 the Lagrange multiplier at each iteration  $k$  using dichotomy.

332 Additional tools are classically introduced in the topology optimization algorithm in order  
 333 to improve stability and convergence properties. In particular, a filter that aims at smoo-  
 334 thing density evolutions between neighboring elements (nonlocal effect) is employed [17].  
 335 In the following, we use a filtering technique defined from a convolution matrix with terms  
 336  $\widehat{H}(e, e^*) = \langle r_{min} - dist(e, e^*) \rangle_+$ ,  $e$  and  $e^*$  denoting two elements of the grid, and  $r_{min}$  being  
 337 the maximal distance where  $\widehat{H}$  is non-zero (i.e. parameter that selects the spatial influence  
 338 of the filter). Gradients of the cost function are then weighted (from distances between  
 339 elements) and changed as :

$$\widehat{\frac{\partial c}{\partial \rho_e}} = \frac{1}{\rho_e \sum_{e^*=1}^{N_e} \widehat{H}(e, e^*)} \sum_{e^*=1}^{N_e} \widehat{H}(e, e^*) \rho_{e^*} \frac{\partial c}{\partial \rho_{e^*}} \quad (23)$$

340 A sketch of the resulting global topology optimization algorithm is given in Fig. 2. For  
 341 this latter algorithm, the initial guess is usually chosen as  $\rho_e = f_v$  for all  $e$  (homogeneous  
 342 material distribution). An illustrative example of the application of the algorithm is given  
 343 in AppendixA.

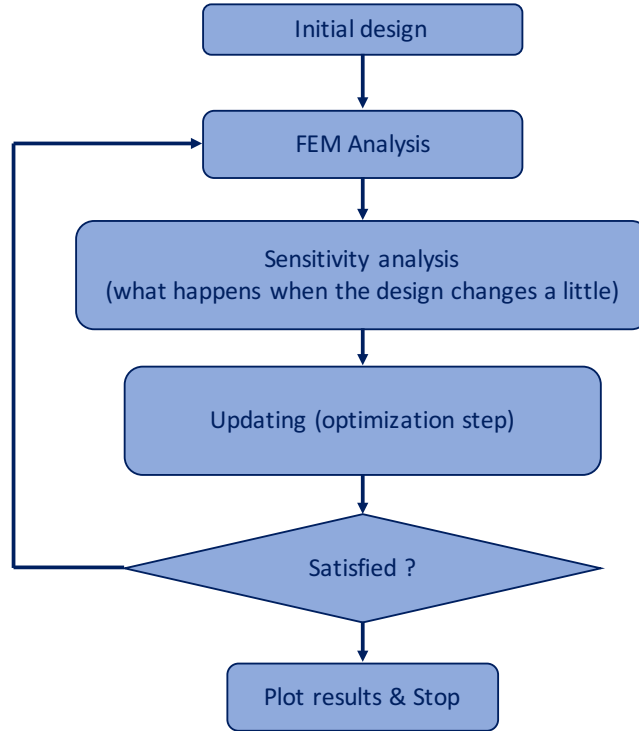


FIGURE 2: Global algorithm for topology optimization.

344 *3.1.3. Illustrative comments on the cost function*

345 We now briefly investigate the mathematical properties of the cost function  $c(\boldsymbol{\rho})$  defi-  
 346 ned in (20) from the structural compliance. The goal here is to highlight the theoretical  
 347 background that makes classical topology optimization mathematically sound, in order to  
 348 address the design of a convenient cost function when coupling with the DIC-FEMU proce-  
 349 dure presented in Section 2.

350 To keep the analysis simple and analytical, we consider a 1D problem. It consists in a set  
 351 of three beams of same length  $L$  and section  $S$ , clamped at  $x = 0$  and subject to a global  
 352 traction loading  $F$  at  $x = L$  (Fig. 3). The Young modulus of the structural material is  
 353 denoted  $E$ , while density variables are denoted  $\rho_1$  (central beam) and  $\rho_2$  (top and bottom  
 354 beams, using symmetry). Consequently, the vector of density variables is  $\boldsymbol{\rho} = [\rho_1, \rho_2]^T$  and  
 355 the volume fraction constraint reads  $\frac{1}{3}(\rho_1 + \rho_2 + \rho_3) = f_v$  in this specific case. The analyti-  
 356 cal solution of the problem leads to the following expression for the compliance cost function

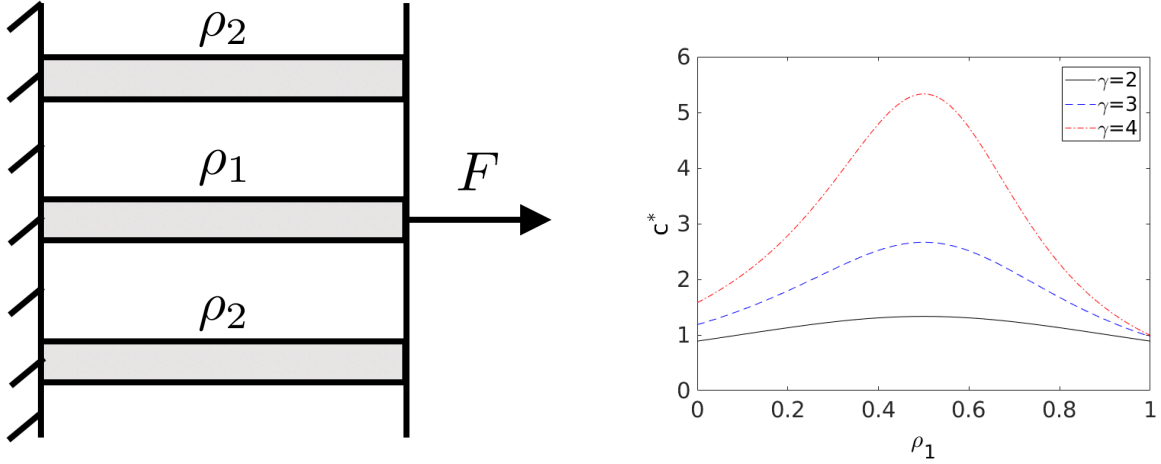


FIGURE 3: Definition of the 1D example (left) and evolution of the cost function  $c^*(\rho_1)$  for several values of  $\gamma$  (right).

357 (using the definition (20)) :

$$c(\rho_1) = \frac{F^2 L}{ES} \frac{1}{\rho_1^\gamma + 2\left(\frac{3f_v - \rho_1}{2}\right)^\gamma} = \frac{F^2 L}{ES} c^*(\rho_1) \quad (24)$$

358 For  $f_v = 0.5$ , the evolution of  $c^*(\rho_1)$  is shown in Fig. 3 with respect to  $\rho_1 \in [\rho_{min}, 1]$  and for  
 359 several values of the penalty factor  $\gamma$  ( $\gamma=2, 3$ , or  $4$ ). We clearly observe that the shape and  
 360 gradients of  $c(\rho_1)$  over the constrained space  $[\rho_{min}, 1]$  (or  $[\rho_{min}, 1]^{N_e-1}$  in the general case)  
 361 naturally drives density variables close to 0 or 1, which is beneficial for the stability and  
 362 convergence of the topology optimization algorithm.

### 363 3.2. Procedure for topology optimization dedicated to parameter identification

#### 364 3.2.1. General idea

365 We now wish to use topology optimization for the design of specimen that optimize  
 366 performance in specific parameter identification. The goal is that, for such specimen, hete-  
 367 rogeneity be created from an unconventional geometry, and the measured displacement field  
 368 be highly sensitive to the constitutive parameters of interest. This requires the setting of  
 369 a scalar cost function which is related to sensitivity with respect to these parameters. For  
 370 that purpose, sensitivity fields which are available once the identification process has been

371 performed constitute rich information; they indicate where the experiment is sensitive to  
 372 parameters.

373 **Remark 6.** It is important to recall that sensitivity fields  $\mathbb{S}_{\mathbf{p}} = \partial \mathbf{U}_s / \partial \mathbf{p}$  can be computed  
 374 before performing any experiment. Their computation is based on FE analysis and the finite  
 375 difference method (see (11)). This leads to fields initially defined at each node of the mesh,  
 376 which can then be interpolated over the spatial domain using various approaches. We also  
 377 note that alternative numerical strategies providing an efficient derivation of sensibility fields  
 378 may be found, such as those based on virtual body forces or on reduced order modeling [50,  
 379 51]; they are not considered here.

380 As explained in Section 2.2, uncertainty in the parameter identification performed from  
 381 DIC-FEMU (or I-DIC) can be minimized by maximizing eigenvalues  $\lambda_i^H$  of the Hessian  
 382 matrix  $\mathbb{H}_{FEMU} = \mathbb{S}_{\mathbf{p}}^T \mathbb{C}_U^{-1} \mathbb{S}_{\mathbf{p}}$  which is related to sensitivity fields. Consequently, when consi-  
 383 dering identification of a single parameter  $p$ , the cost function  $c(\boldsymbol{\rho})$  to be minimized in the  
 384 topology optimization algorithm should involve  $1/\lambda^H$  with  $\lambda^H = \mathbb{S}_p^T \mathbb{C}_U^{-1} \mathbb{S}_p$ . In the case of  
 385 multiparameter identification such as performed in [55], a choice is to involve  $1/\min(\lambda_i^H)$   
 386 or  $\max(\lambda_i^H)/\min(\lambda_i^H)$  depending on boundary conditions [28, 15]. These two quantities are  
 387 equivalent when the maximal displacement is given in the problem, but the second one  
 388 avoids divergence issues in the contrary case (e.g. free boundaries). An alternative choice is  
 389 to involve  $1/\det(\mathbb{H}_{FEMU}) = 1/\prod_i \lambda_i^H$ . We point out that the choice of cost function, when  
 390 considering multi-parameter identification, is fundamental as it will lead to different optimi-  
 391 zed topologies with compromise between sensitivities to each individual parameter (see the  
 392 illustration in AppendixA.2 for classical topology optimization).

393 An illustration of the use of eigenvalues of the Hessian matrix in a cost function is given  
 394 in AppendixB; it is implemented for simpler shape optimization with few design variables.

395  
 396 When dealing with topology optimization, we propose to replace the initial algorithm  
 397 described in Fig. 2 with a new one described in Fig. 4. In this new algorithm, the FE analysis

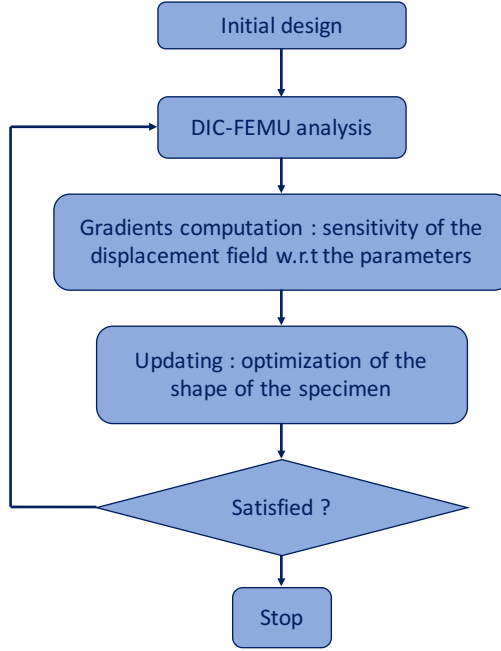


FIGURE 4: New algorithm for topology optimization dedicated to optimal parameter identification.

398 (that classically computes structural stiffness/compliance, or effective properties of a micro-  
 399 structure) is replaced with a (DIC-)FEMU or I-DIC analysis in order to compute sensitivity  
 400 fields and eigenvalues of the Hessian matrix  $\mathbb{H}_{FEMU}$  to be used in the cost function. These  
 401 are recomputed each time the specimen geometry changes in the iterative algorithm. Other  
 402 parts of the algorithm (optimization method, filtering procedure) are kept unchanged. The  
 403 meaning of the density vector  $\boldsymbol{\rho}$  is also unchanged (it does not refer to densities of measure-  
 404 ments). As material density variables  $\rho_e$  are used to compute the FE displacement  $\mathbf{U}_s$ , they  
 405 are naturally involved as weights in the definition of sensitivity fields.

406 **Remark 7.** To avoid any misleading, we will refer to gradients rather than sensitivities  
 407 (which are already used in FEMU) when dealing with derivatives of the cost function  $c(\boldsymbol{\rho})$   
 408 with respect to elementary density variables  $\rho_e$ . Usually, there is no analytical expression  
 409 of these gradients when merging topology optimization with DIC-FEMU, due to a complex  
 410 and implicit relation between the cost function  $c$  and density variables. In practice, gradients  
 411 will be numerically computed using a finite difference approximation.

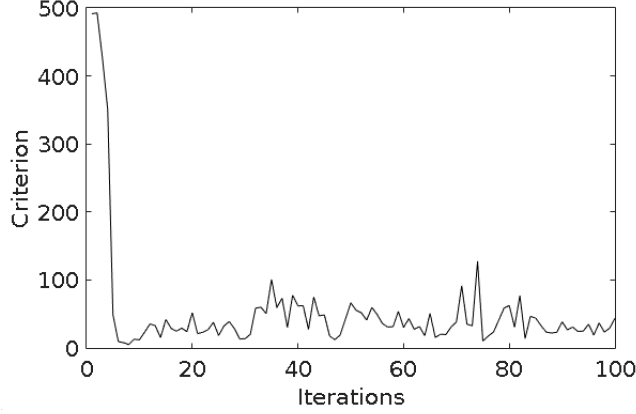


FIGURE 5: Evolution of the cost function with respect to iterations.

412 **Remark 8.** In this pre-conception phase of the specimen, the matrix  $\mathbb{C}_U^{-1}$  is unknown as no  
 413 full-field measurement is available. For the computation of the Hessian matrix, it is replaced  
 414 with  $\overline{\mathbb{C}}_U^{-1} = (1/2\gamma_f^2) \sum_e \mathbb{N}^T \mathbb{N}$  (mean field approximation).

### 415 3.2.2. Setting convenient cost functions

416 We now wish to design convenient cost functions that enable stability and convergence in  
 417 the topology optimization process when dealing with parameter sensitivity. In this context,  
 418 it is important to recover similar mathematical properties as these exhibited in Section 3.1.3  
 419 when dealing with classical topology optimization. Indeed, considering again the 2D traction  
 420 test shown in Fig. 1 and optimizing sensitivity with respect to the shear modulus  $G_{12}$ , a  
 421 natural choice of the cost function  $c(\boldsymbol{\rho}) = \frac{1}{\mathbb{S}_{G_{12}}^T \overline{\mathbb{C}}_U^{-1} \mathbb{S}_{G_{12}}}$  leads to the convergence curve shown  
 422 in Fig. 5. We observe oscillations which are due to the fact that the previous cost function  
 423 is far from concave, with slight changes around local minima for some ranges of density  
 424 variables. This favors the occurrence of gray zones in the optimized topology, with unstable  
 425 effects and convergence difficulties. Consequently, enhancements should be introduced in the  
 426 definition of  $c(\boldsymbol{\rho})$  to get better numerical properties.

427

428 In order to come back to the convenient mathematical background of classical topology  
 429 optimization, we propose to introduce in the cost function a penalization term that forces

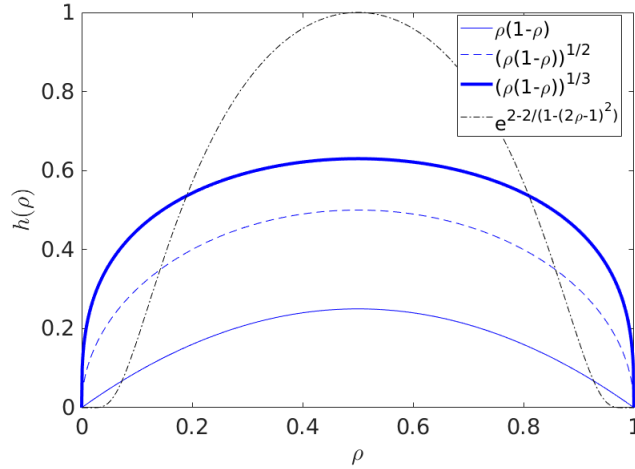


FIGURE 6: Plot of various possible penalization functions  $h(\rho)$  over  $[\rho_{min}, 1]$ .

430 density variables to go close to 0 or 1. It is chosen of the form (for a single identified  
 431 parameter) :

$$c(\boldsymbol{\rho}) = \frac{1}{\lambda^H} + \kappa \sum_{e=1}^{N_e} \exp \left( 2 - \frac{2}{1 - (2\rho_e - 1)^2} \right) \quad (25)$$

432 The chosen penalization function  $h(\rho) = \exp \left( 2 - \frac{2}{1 - (2\rho - 1)^2} \right)$  in each element is plotted in  
 433 Fig. 6. The obtained bell curve allows : (1) a clearer material distribution by forcing density  
 434 variables to go close to 0 or 1 ; (2) possible changes for density variables that would initially  
 435 be close to 0 or 1, as it exhibits small gradients close to 0 or 1, contrary to alternative  
 436 possible penalization functions such as  $h^*(\rho) = [\rho(1 - \rho)]^r$  which present stronger gradients  
 437 in these regions (Fig. 6). In other words, we choose here a regularization that proposes an  
 438 essential singularity in 0 and 1 ( $h$  and  $h^{(n)}$  vanish at these points), which prevents from  
 439 degeneration ranges in density.

440 The scalar penalty parameter  $\kappa$  in (25) should be conveniently chosen, as in any pena-  
 441 lization method, to obtain smooth convergence. In the following, it will be chosen constant  
 442 along the optimization process (even though it could also be dynamically changed, and in  
 443 particular increased at the end of the process to force binarity and clean the optimized  
 444 geometry). Furthermore, the initial configuration of the material distribution should also  
 445 conveniently set in order to converge to a global minimum. These aspects will be addressed

446 in Section 4 from numerical experiments.

## 447 4. Numerical results

448 In this section, we design and analyze performance of the proposed approach on several  
449 numerical experiments. They are all based on two-dimensional test-cases with linear elastic  
450 materials and plane stress assumption. During the iterative process described in Fig. 4,  
451 gradients of  $c(\boldsymbol{\rho})$  were obtained using the finite difference method. For each elementary  
452 density, we thus considered  $\partial c/\partial \rho_e \approx (c(\boldsymbol{\rho} + \delta \rho_e \mathbf{I}_e) - c(\boldsymbol{\rho}))/\delta \rho_e$  with  $\mathbf{I}_e$  the vector of size  $N_e$   
453 with component 1 in line  $e$  and 0 elsewhere, and we chose  $\delta \rho_e = 0.001$  in practice.

454 All numerical results dealing with topology optimization were obtained from a home-made  
455 Matlab software, while the Correli software (under patent [44]) was used to perform DIC.

### 456 4.1. Optimization for Young's modulus identification in a uniaxial case

457 For validation purposes, we first consider a simple case where the goal is to identify  
458 the Young modulus  $E$  of an isotropic material alone from a uniaxial test (see Figure 7  
459 where boundary conditions are indicated). The topology optimization procedure starts with  
460 a random distribution of the material inside a rectangular domain split in  $40 \times 20$  squared  
461 elements of equal size. We choose  $\kappa = 0$  (no penalization),  $\gamma = 3$ , and  $f_v = 0.6$ . Consequently,  
462 the cost function which is considered for topology optimization reads :

$$c(\boldsymbol{\rho}) = \frac{1}{\mathbf{S}_E^T \overline{\mathbf{C}}_U^{-1} \mathbf{S}_E} \quad (26)$$

463 Along the iterations, this cost function is decreased by modifying the material distribution  
464 and the approach tends, as expected, to the rectangular optimal shape with homogenous  
465 material density (equal to 0.6). The material distribution is shown in Figure 7 for different  
466 iterations of the algorithm.

467 We observe in Figure 8 that a large increase (factor  $10^4$ ) in the sensitivity is then obtained,  
468 so that the performance of FEMU identification is optimized. We also observe that the  
469 convergence of the topology optimization method is very fast as the optimized shape is

470 reached after 5 iterations only. Similar results were obtained from alternative initial material  
 471 distributions.

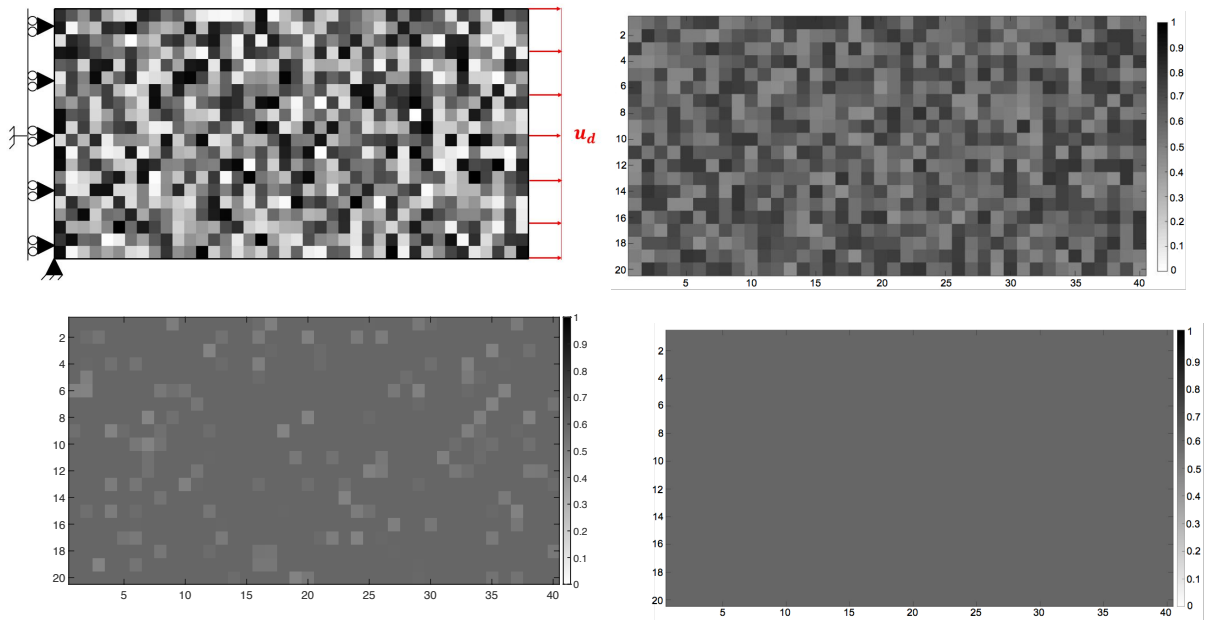


FIGURE 7: Initial configuration with boundary conditions (top left), and material distribution at iteration 2 (top right), iteration 4 (bottom left), and iteration 5 (bottom right).

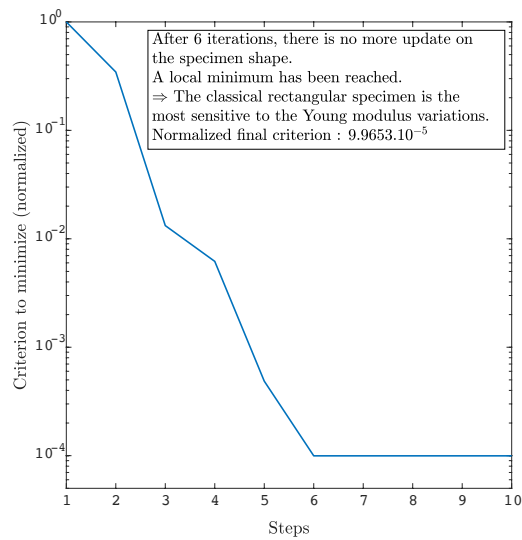


FIGURE 8: Evolution of the value of the cost function along the iterations of the algorithm.

472 *4.2. Realistic application with experimental validation*

473 We now consider a two-dimensional traction test-case with orthotropic linear elastic  
 474 material such as defined in Fig. 1. The orthotropy direction is assumed to be uniformly  
 475 distributed and fixed during the optimization procedure. The identified material parameter is  
 476 here the shear modulus  $G_{12}$  alone, which is a quite complex parameter to identify in practice.  
 477 Consequently, the cost function which is considered for topology optimization reads :

$$c(\boldsymbol{\rho}) = \frac{1}{\mathbb{S}_{G_{12}}^T \overline{\mathbb{C}}_U^{-1} \mathbb{S}_{G_{12}}} + \kappa \sum_{e=1}^{N_e} \exp \left( 2 - \frac{2}{1 - (2\rho_e - 1)^2} \right) \quad (27)$$

478 *4.2.1. Setting parameters of the cost function*

479 We first investigate the setting or parameters  $\gamma$  and  $\kappa$ , in order to define the best couple  
 480 of values in terms of convergence, stability, and contrast in the optimized geometry. As an  
 481 initial guess, we consider a rectangular geometry of the specimen in which material density  
 482 is homogeneous and equal to  $f_v$ . It is split in  $30 \times 15$  squared elements of equal size. Out of  
 483  $G_{12}$  to be identified, material parameters are set to  $E_1 = E_2 = 1$ , and  $\nu_{12} = 0.3$ .

484 The filter parameter is set to  $r_{min} = 1.5$ . Considering  $f_v = 0.6$ , we take  $\gamma$  in the range  $[2, 3, 4]$   
 485 and  $\kappa$  in the range  $[0.01, 0.1, 1]$ . Optimization results are reported in Fig. 9; they show the  
 486 convergence of the cost function along the iterations, for several configurations. We observe  
 487 that selecting  $\kappa = 0.1$  and  $\gamma = 3$  seems to be the best option; we will consider this couple of  
 488 values in the remainder of this section. We also indicate that taking  $\gamma = 1$  would give here  
 489 very poor results, so that the joint use of the penalization function (introduced in Section  
 490 3.2.2) and the power law (classically used in the SIMP approach) seems mandatory.

491 Keeping the same example, we now investigate the choice of the initial guess in the opti-  
 492 mization algorithm, as it may influence the obtained solution (with convergence to specific  
 493 local or global minima). We analyze three cases (see Fig. 10) :

- 494 — random material distribution;
- 495 — checkerboard material distribution;
- 496 — uniform material distribution.

497 Results obtained from these three cases of initial conditions are reported in Fig. 11; they  
 498 show similar patterns in the obtained optimal material distribution. Furthermore, the diffe-

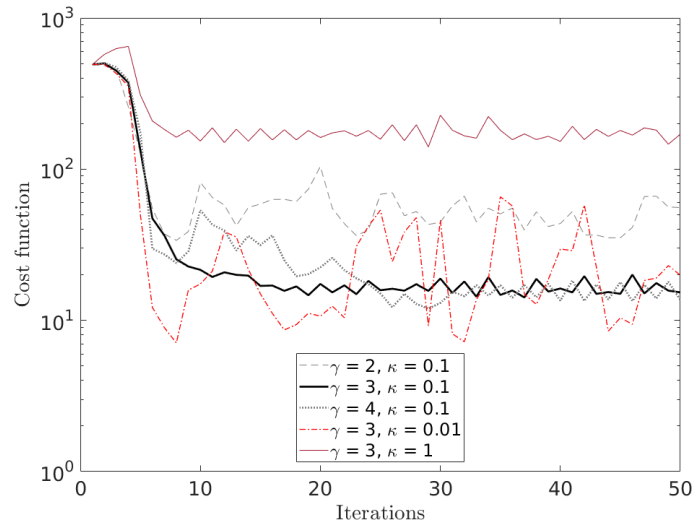


FIGURE 9: Results obtained for several sets of parameters  $(\gamma, \kappa)$  using a logarithmic vertical scale.

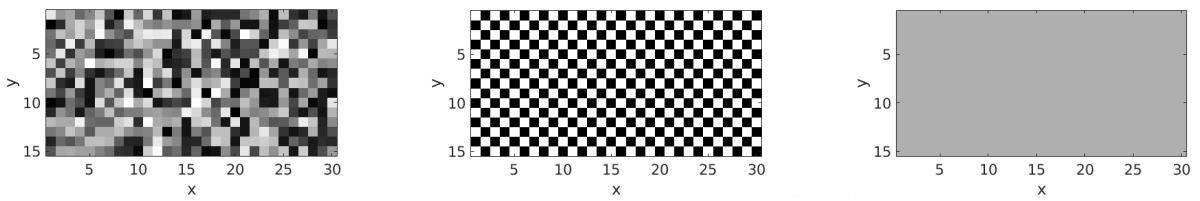


FIGURE 10: The three material distributions used as initial guess : random, checkerboard, uniform (from left to right).

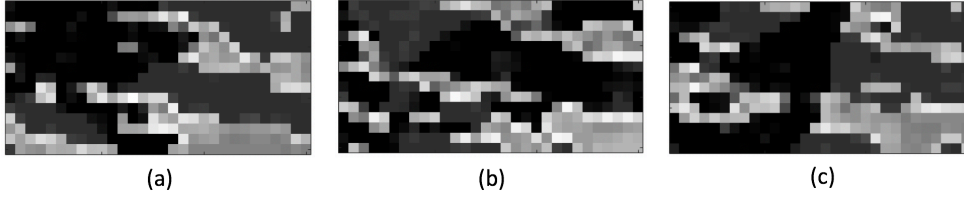


FIGURE 11: Optimal material distribution obtained from the three investigated initial conditions : (a) random material distribution ; (b) checkerboard material distribution ; (c) uniform material distribution.

599 rence in the final value of the cost function for the three cases is under 3%. This consolidates  
 500 the opinion on the robustness of the approach. We will consider a checkerboard material  
 501 distribution as the initial guess in the remainder of this section.

#### 502 4.2.2. Full optimization of the specimen

503 With the previously set parameters of the method, we now consider the maximization  
 504 of sensitivity with respect to the shear modulus  $G_{12}$  on a working space discretized with  
 505  $50 \times 25$  squared elements of equal size. Considering  $f_v = 0.8$ , the optimization results are  
 506 shown in Fig. 12. We display sensitivity fields  $\frac{\partial \mathbf{U}}{\partial G_{12}} \cdot \mathbf{e}_1$  and  $\frac{\partial \mathbf{U}}{\partial G_{12}} \cdot \mathbf{e}_2$ , along directions  $\mathbf{e}_1$  and  
 507  $\mathbf{e}_2$  respectively, for the optimized specimen. We note that the optimized geometry (density  
 508 map) has been filtered for representation. The CPU time to obtain this optimized topology  
 509 was about 10 hours on a laptop with single processor. Nevertheless, and even though it is  
 510 not the focus of the paper, it could be easily decreased by further optimizing the numerical  
 511 procedure (for instance by interpolating gradients between selected computed points) or  
 512 resorting to parallel computing for the computation of the gradients.

513 We observe that the optimized specimen is very sensitive to  $G_{12}$ , even though there is a  
 514 lack of physical meaning with a small part of material which is not linked to the remainder  
 515 of the structure after filtering (in the non-filtered geometry, there were low densities which  
 516 were removed after filtering).

#### 517 4.2.3. Experimental validation of the optimized specimen geometry

518 In this last section, we perform the experimental validation of the optimized specimen ob-  
 519 tained in Section 4.2.2. Contrary to previous studies in which measurements were synthetic,

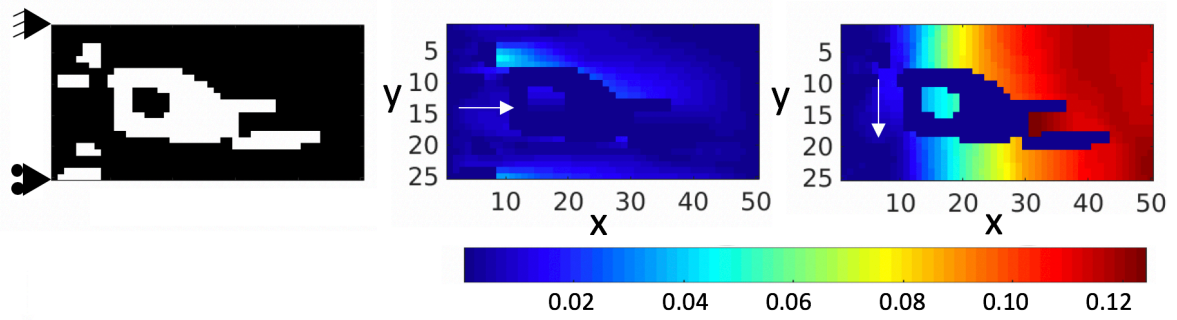


FIGURE 12: Geometry (left) and sensitivity fields with respect to  $G_{12}$  (center and right) obtained from the optimized specimen.

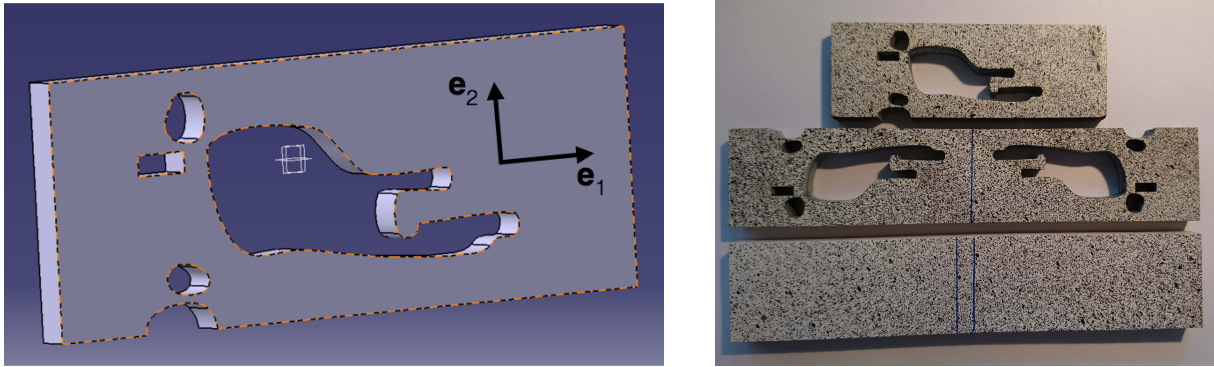


FIGURE 13: CAD model of the optimized specimen using CATIA (left) and manufactured specimen with applied speckle (right).

520 we now set up an experimental test from the optimized specimen and boundary conditions  
 521 defined in the numerical analysis. We then apply the DIC-FEMU procedure for parameter  
 522 identification.

523

524 A first step is to manufacture the specimen. For this purpose, and starting from the  
 525 optimized solution given by the optimization methodology (global idea of the final manufac-  
 526 turable structure), a further step of transfer of the solution into a CAD model is required.  
 527 This is performed using the Catia software, which gives the CAD model shown in Fig. 13.  
 528 The geometry, which is not conventional, can then be realized using a laser cutting machine.  
 529 We point out here that a filtered geometry was considered, removing the internal isolated  
 530 region for manufacturing issues, and therefore slightly modifying the volume fraction. The

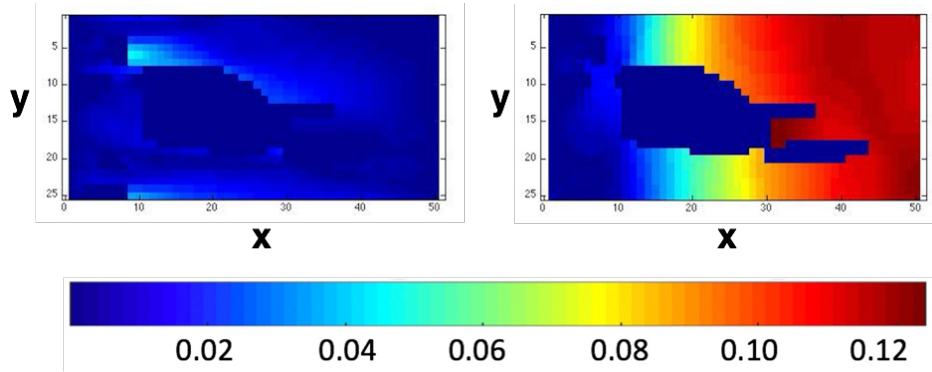


FIGURE 14: Sensitivity fields with respect to  $G_{12}$  obtained after removing the internal isolated region from the optimized specimen.

531 associated sensitivity fields are shown in Fig. 14; they are very similar to those shown in  
 532 Fig. 12 for the original optimized topology, and the corresponding change in the cost function  
 533 value (normalized by the volume fraction) is then less than 2%.

534 The chosen orthotropic material is fir wood (which is quite homogeneous) and wood  
 535 parts without any apparent defect are carefully selected in order to be in line with a uniform  
 536 distribution of orthotropy directions; the orientation of wood fibers then corresponds to  
 537 an orthotropy direction. Full classical specimen are also constructed in order to perform  
 538 comparisons in sensitivities. The obtained specimens, with a speckle applied on faces, are  
 539 shown in Fig. 13.

540 The second step consists in applying DIC to the specimens in order to obtain a measured  
 541 displacement field. An INSTRON compression machine is used to perform tests (Fig. 15). In  
 542 practice, boundaries of the specimen are clamped on the jaws during the experimental test.  
 543 Therefore, in order to reproduce similar boundary conditions as in the traction numerical  
 544 test (with free vertical displacement on the right side, see Fig. 1), it is chosen to double the  
 545 specimen and to use symmetry properties to recover such boundary conditions experimen-  
 546 tally.

547 A Nikon 24.5 objective is used on the camera with  $700 \times 300$  pixels and a pixel size of  $100 \mu\text{m}$ .  
 548 The analysis of a first set of 10 unloaded images enables one to recover the initial state and  
 549 information on the measurement noise. DIC is then performed from the Correli software [35].

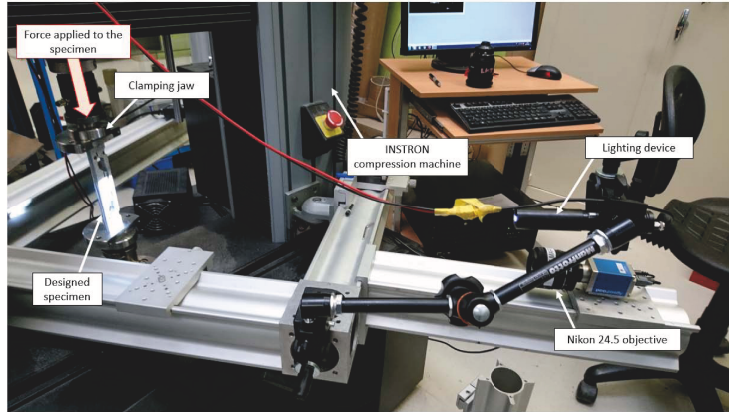


FIGURE 15: Experimental device used for DIC.

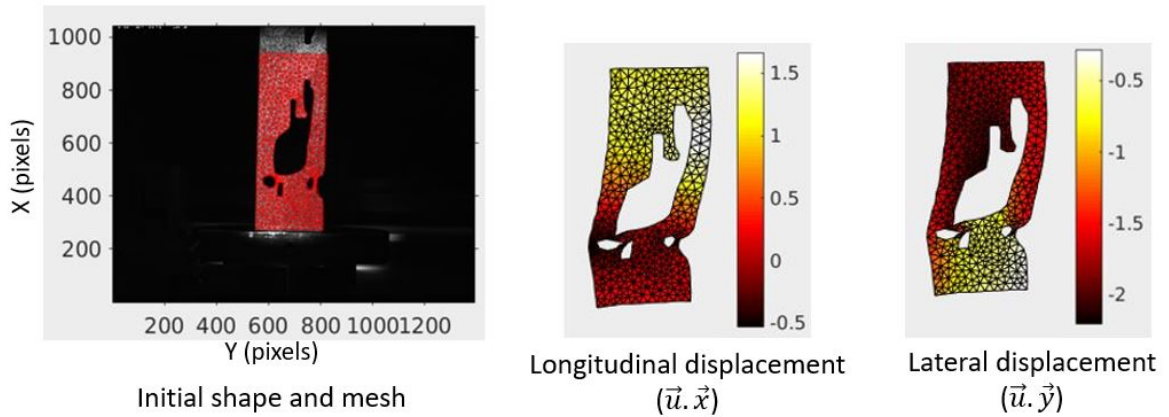


FIGURE 16: Results of the DIC process : mesh (left), and longitudinal and lateral displacements (center and right) projected on the deformed geometry (with amplification) of the optimized specimen.

550 The obtained displacement field (transverse component) for the optimized and doubled spe-  
 551 cimen is given in Fig. 16 ; it illustrates the originality of the designed specimen, which creates  
 552 dissymmetric and heterogenous fields.

553 The third and last step consists in identifying the material parameter  $G_{12}$  using the  
 554 FEMU approach (see Section 2.2). The displacement field and boundary conditions extrac-  
 555 ted from DIC are used to drive the identification process.

556 Running the identification process then requires to minimize the FEMU cost function. The  
 557 plot of this (normalized) cost function with respect to the value of  $G_{12}$  is reported in Fig. 17,

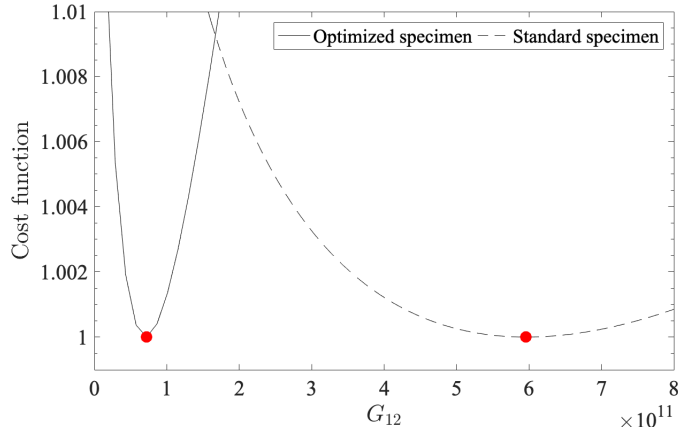


FIGURE 17: Evolution of the cost function (normalized with its minimum, and with log scale on the vertical axis) with respect to  $G_{12}$ , for the optimized specimen (left) and the full standard specimen (right).

558 for both optimized and standard (i.e. rectangular) specimens. It is interesting to notice that  
 559 in the standard case, due to the compression test realized, a minimum of the cost function  
 560 should not exist as the shear modulus  $G_{12}$  can not be identified from a pure uniaxial trac-  
 561 tion/compression test along a main direction of orthotropy. However, imperfect experimental  
 562 boundary conditions coming from DIC are used for the numerical simulations in FEMU, so  
 563 that a uniaxial compression is not simulated in practice (bias in the symmetry) and a low  
 564 sensitivity to shear is found; however, it is 2000 times smaller than that of the optimized  
 565 specimen.

566 From Fig. 17, we also notice that the uncertainty (or confidence interval) on the identified  
 567 parameter is very small for the optimized specimen compared to the standard specimen;  
 568 this is shown by the strong curvature around the minimum of the cost function. The clear  
 569 minimum obtained for identification from the optimized specimen is in accordance with the  
 570 initial objective of the work. It shows that topology optimization in the context of parame-  
 571 ter identification and with a cost function related to sensitivity fields is both relevant and  
 572 effective. Indeed, if a FEMU method were to be implemented from the optimized specimen  
 573 (using in practice a gradient descent), it would converge much faster as the gradient of the  
 574 curve, which is the FEMU sensitivity, is much steeper.

575 *4.3. Optimization for multi-parameter identification*

576 As a last example, and in order to show the robustness of the method, we apply the  
 577 optimization algorithm for a specimen dedicated to the identification of several material  
 578 parameters. The considered mechanical problem is similar to that considered in Section 4.2,  
 579 with a homogeneous orthotropic behavior and a pure traction loading with prescribed longi-  
 580 tudinal displacement on the right side (see Figure 7). However, the four material parameters  
 581  $E_1$ ,  $E_2$ ,  $\nu_{12}$ , and  $G_{12}$  are now identified from full-field measurements. The cost function which  
 582 is chosen reads :

$$c(\boldsymbol{\rho}) = \frac{1}{\min(\lambda_i^H)} + \kappa \sum_{e=1}^{N_e} \exp \left( 2 - \frac{2}{1 - (2\rho_e - 1)^2} \right) \quad (28)$$

583 where  $\lambda_i^H$  are eigenvalues of the Hessian matrix  $\mathbb{H}_{FEMU} = \mathbb{S}_{\mathbf{p}}^T \overline{\mathbb{C}}_U^{-1} \mathbb{S}_{\mathbf{p}}$ . We choose  $\kappa = 0.5$ ,  
 584  $\gamma = 3$ , and  $f_v = 0.8$ .

585 Splitting the initial rectangular domain in  $30 \times 15$  squared elements of equal size, results  
 586 of the optimization algorithm are given in Fig. 18. They show a fast convergence of the  
 587 procedure (the asymptotic regime is reached after 12 iterations only), with a final sensitivity  
 588 of the specimen increased by a factor 10. Moreover, the algorithm leads to a physically  
 589 acceptable material distribution, i.e. optimal specimen geometry, as it indicates that the  
 590 regions of the working space which need to be considered as solid (black zones in Figure 18)  
 591 are located along the upper and lower boundaries (which is consistent with the identification  
 592 of Young moduli) as well as along 3 bands with 45-degree angle (which is consistent with  
 593 the identification of the shear modulus). The white and light grey zones would be removed  
 594 when manufacturing the optimal specimen.

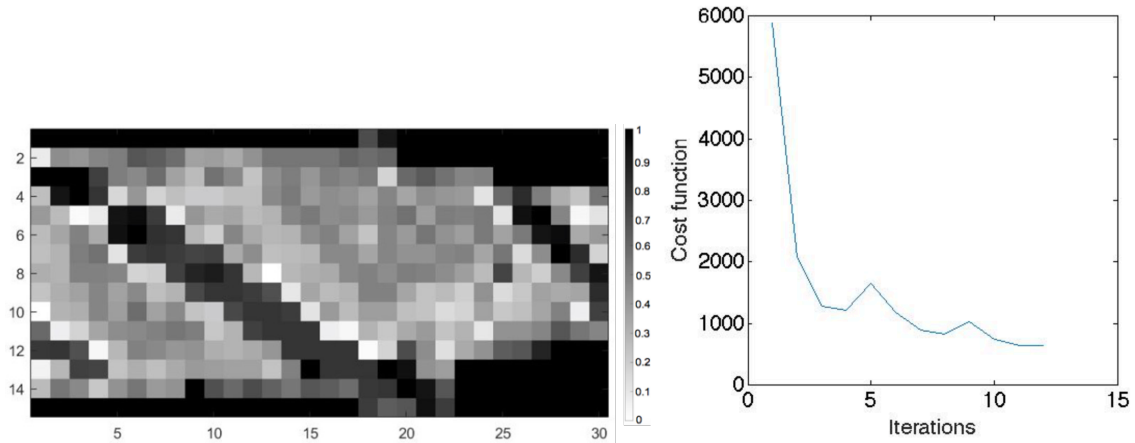


FIGURE 18: Optimal material distribution obtained at convergence (left), and evolution of the value of the cost function along the iterations of the algorithm.

## 595 5. Conclusions and prospects

596 In this paper, we investigated the use of topology optimization in order to optimize  
 597 sensitivity when performing parameter identification from the DIC-FEMU framework. We  
 598 described in details how the implementation could be performed, focusing in particular on a  
 599 convenient definition of the optimality criterion. Numerical results and experimental valida-  
 600 tion confirmed the performance of the approach. The research work thus appears as a novel  
 601 contribution in the literature of full-field measurements and topology optimization, provi-  
 602 ding a practical tool of interest for engineers investigating experimental design and willing  
 603 to optimize the quality of information extracted from their experimental campaign. Never-  
 604 theless, the proposed procedure is associated with several limitations which were pointed  
 605 out in the numerical results. In particular, numerical parameters should be conveniently set  
 606 to ensure fast convergence, numerical costs may be high, and there is a strong issue to tackle  
 607 regarding the physical feasibility of some shapes provided by the method. Consequently,  
 608 the proposed method paves the way for further research studies that may circumvent these  
 609 current limitations; we can list :

- 610 — the use of other topology optimization procedures such as those based on level sets [3] ;
- 611 — the use of alternative optimization algorithms, such as those based on stochastic

612 formulations (simulated annealing method, genetic algorithms, ...) which are suited  
613 to problems with very high multiplicity of minima and with a hierarchical structure.  
614 These may be simpler to implement (no computation of gradients) and may avoid  
615 geometry filtering, but they also may lead to a larger number of iterations ;  
616 — the implementation of relaxation techniques to further improve convergence proper-  
617 ties of the optimization process ;  
618 — the introduction of additional constraints in the cost function, related for instance  
619 to the maximal admissible stress in the structure (avoid tiny parts), to machining  
620 capabilities and manufacturing constraints [67, 4, 5], or to smoother boundaries of  
621 the optimized specimen with control of curvatures ;  
622 — the application of the procedure to nonlinear material behaviors such as plasticity.  
623 In this context, tools exist to directly link IDIC in Correli 3.0 with the Abaqus  
624 software [44] ; they could be advantageously used ;  
625 — the use of reduced order modeling (ROM) techniques in order to improve computa-  
626 tional costs, as initiated in [50] or discussed in [51].  
627 All these aspects will be the topics of forthcoming research works.

## 628 **Acknowledgements**

629 The authors thank Stéphane Roux (LMT, ENS Paris-Saclay) for the fruitful discussions  
630 on the topic and helpful comments and advice, which enhanced the quality of the work.

## 631 **AppendixA. Illustrative implementations of the SIMP topology optimization** 632 **algorithm**

### 633 *AppendixA.1. Influence of the algorithm parameters*

634 We consider a simple example on a working space defined as a cantilever beam (Fig. A.19).  
635 It is clamped on the left and submitted to a unit flexion force on its bottom right corner.  
636 The remainder part of the domain boundary is free. Defining the volume fraction  $f_v = 0.5$ ,  
637 the iterative algorithm leads to the optimized geometry given in Fig. A.19. We also illustrate

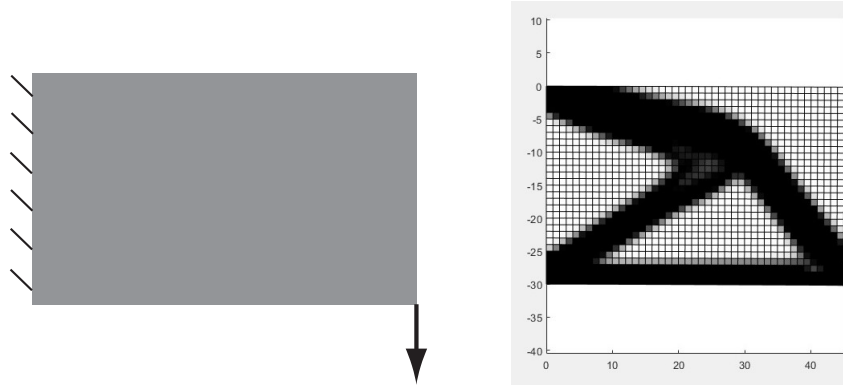


Figure A.19: Illustrative problem with optimal geometry defined from topology optimization.

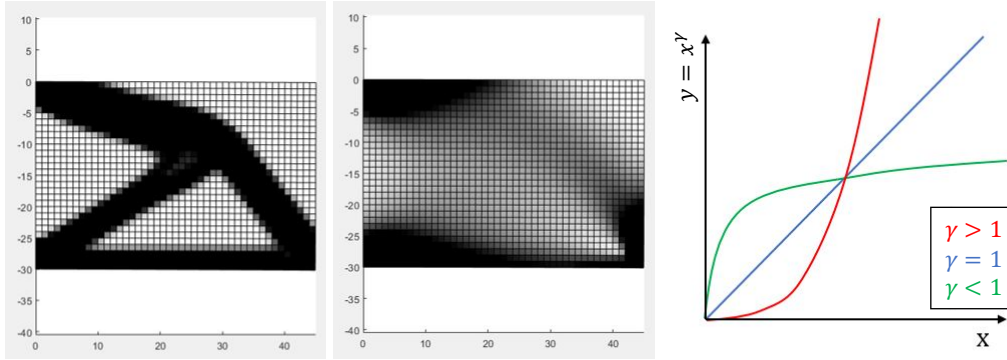


Figure A.20: Influence of the penalty factor on the optimized geometry, with  $\gamma = 5$  (left) and  $\gamma = 0.5$  (right).

638 in Fig. A.20 and Fig. A.21, respectively, the influence of the penalty factor (with  $\gamma = 5$  and  
 639  $\gamma = 0.5$ ) and the filtering process (with several values of  $r_{min}$ ).

#### 640 *Appendix A.2. Influence of the optimality criterion*

641 The choice of optimality criterion is fundamental as it will lead to different optimized  
 642 topologies. This is illustrated in Fig. A.22 when using topology optimization to maximize  
 643 one the three inertia moments in a square domain:

$$I_x = \int_{\Omega} \mu y^2 d\Omega \quad I_y = \int_{\Omega} \mu x^2 d\Omega \quad I_z = \int_{\Omega} \mu (x^2 + y^2) d\Omega \quad (\text{A.1})$$

644 with given volume fraction  $f_v = 0.5$ .

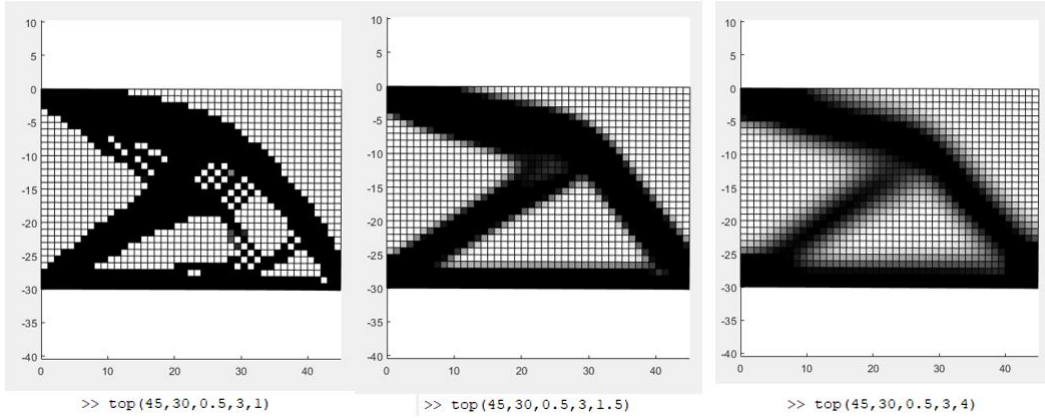


Figure A.21: Impact of the filtering on the optimized geometry, with  $r_{min} = 1$  (left),  $r_{min} = 1.5$  (center), and  $r_{min} = 4$  (right).



Figure A.22: Optimization results with respect to inertia moments  $I_x$  (left),  $I_y$  (center), and  $I_z$  (right).

## 645 AppendixB. Optimal placement of a hole in a plate

646 We perform optimization of parameter sensitivity using few design variables, not a large  
 647 amount of density variables as in the general topology optimization methodology. The  
 648 goal is to ensure that the connexion between DIC-FEMU (that defines the cost function)  
 649 and a standard minimization algorithm is correctly set. Consequently, we perform shape  
 650 optimization rather than topology optimization here.

651 We consider a rectangular specimen, made of an isotropic linear elastic material, in which  
 652 a hole is created. The objective is to define the radius  $r$  and the position  $(d_1, d_2)$  (in the  
 653 Cartesian coordinate system  $(O, \mathbf{e}_1, \mathbf{e}_2)$ ) of the center of the hole so that the sensitivity with  
 654 respect to the Poisson ratio  $\nu$  (or the Young modulus  $E$ ) is maximized. From the FEMU  
 655 Hessian matrix, we thus define the following cost function depending on the design variables

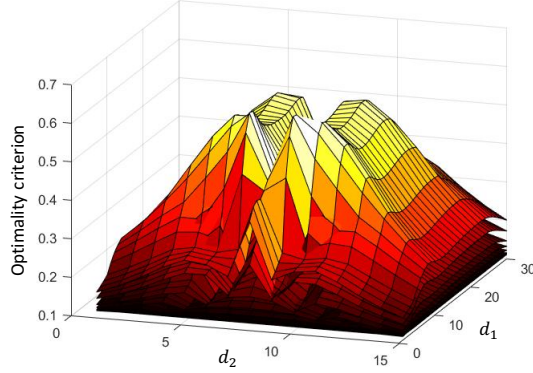


Figure B.23: Map of the optimality criterion over the space  $(d_1, d_2)$ , for several values of  $r$ .

656 set  $\mathbf{q} = [d_1, d_2, r]^T$ :

$$c(\mathbf{q}) = \frac{1}{\mathbf{S}_\nu^T \mathbf{C}_U^{-1} \mathbf{S}_\nu} \quad (\text{or} \quad c(\mathbf{q}) = \frac{1}{\mathbf{S}_E^T \mathbf{C}_U^{-1} \mathbf{S}_E}) \quad (\text{B.1})$$

657 The problem then reads:

$$\mathbf{q}_{sol} = \operatorname{argmin}_{\mathbf{q}} c(\mathbf{q}) \quad (\text{B.2})$$

658 The evolution of the optimality criterion  $1/c(\mathbf{q})$  over the design space is given in Fig. B.23;  
 659 each map in the  $(d_1, d_2)$  space corresponds to a fixed value of  $r$  (the upper map corresponds  
 660 to the smallest value of  $r$  considered). We clearly observe that there is a global maximum  
 661 (two from symmetry), which is convenient for the convergence of the optimization algo-  
 662 rithm. In the following, we consider the optimization of the design variables  $(d_1, d_2)$  alone,  
 663 the radius  $r$  being given and fixed. In addition, the design space is restricted to a subset of  
 664 the initial rectangle (with size  $L_1 \times L_2$ ) in order to ensure that the hole fully remains in the  
 665 working physical domain.

666

667 In order to perform minimization of  $c(\mathbf{q})$ , we use a Newton-Raphson algorithm. Intro-  
 668 ducing the variation  $\delta\mathbf{q}$  in the design variables set, a first-order Taylor expansion applied to  
 669 the cost function reads:

$$(c(\mathbf{q} + \delta\mathbf{q}))^2 = \left( c(\mathbf{q}) + \frac{\partial c^T}{\partial \mathbf{q}} \delta\mathbf{q} \right)^T \left( c(\mathbf{q}) + \frac{\partial c^T}{\partial \mathbf{q}} \delta\mathbf{q} \right) = c(\mathbf{q})^2 + 2c(\mathbf{q})\delta\mathbf{q}^T \frac{\partial c}{\partial \mathbf{q}} + \delta\mathbf{q}^T \frac{\partial c}{\partial \mathbf{q}} \frac{\partial c^T}{\partial \mathbf{q}} \delta\mathbf{q} \quad (\text{B.3})$$

670 so that the condition  $\frac{\partial c(\mathbf{q}+\delta\mathbf{q})}{\partial\delta\mathbf{q}} = \mathbf{0}$  yields:

$$c(\mathbf{q})\frac{\partial c}{\partial\mathbf{q}} + \frac{\partial c}{\partial\mathbf{q}}\frac{\partial c^T}{\partial\mathbf{q}}\delta\mathbf{q} = \mathbf{0} \implies \delta\mathbf{q} = -c(\mathbf{q})\left[\frac{\partial c}{\partial\mathbf{q}}\frac{\partial c^T}{\partial\mathbf{q}}\right]^{-1}\frac{\partial c}{\partial\mathbf{q}} \quad (\text{B.4})$$

671 However, numerical experiments show that this approach leads to a badly conditioned sys-  
 672 tem. We thus prefer an alternative approach in which the Taylor expansion is directly  
 673 applied to the sensitivity field. It reads:

$$\mathbb{S}(\mathbf{q} + \delta\mathbf{q}) = \mathbb{S}(\mathbf{q}) + \frac{\partial\mathbb{S}}{\partial\mathbf{q}}\delta\mathbf{q} \quad (\text{B.5})$$

674 so that the cost function becomes:

$$c(\mathbf{q} + \delta\mathbf{q}) = \frac{1}{\left(\mathbb{S}(\mathbf{q}) + \frac{\partial\mathbb{S}}{\partial\mathbf{q}}\delta\mathbf{q}\right)^T \left(\mathbb{S}(\mathbf{q}) + \frac{\partial\mathbb{S}}{\partial\mathbf{q}}\delta\mathbf{q}\right)} \quad (\text{B.6})$$

675 Taking derivative and imposing it to zero leads to:

$$\delta\mathbf{q} = -\left[\frac{\partial\mathbb{S}^T}{\partial\mathbf{q}}\frac{\partial\mathbb{S}}{\partial\mathbf{q}}\right]^{-1}\frac{\partial\mathbb{S}^T}{\partial\mathbf{q}}\mathbb{S}(\mathbf{q}) \quad (\text{B.7})$$

676 At each iteration  $n$  of the optimization algorithm,  $\delta\mathbf{q}^{(n)}$  is computed and the design variables  
 677 set is updated as  $\mathbf{q}^{(n+1)} = \mathbf{q}^{(n)} + \delta\mathbf{q}^{(n)}$ . Iterations are stopped when variations are small i.e.  
 678  $\|\delta\mathbf{q}^{(n)}\| \leq \epsilon$  where  $\epsilon$  is a given value.

679

680 We apply the algorithm for a radius  $r = L_2/6$ . Results are given in Fig. B.24; we show the  
 681 evolution of the hole position and that of the value of the cost function along the iterations.

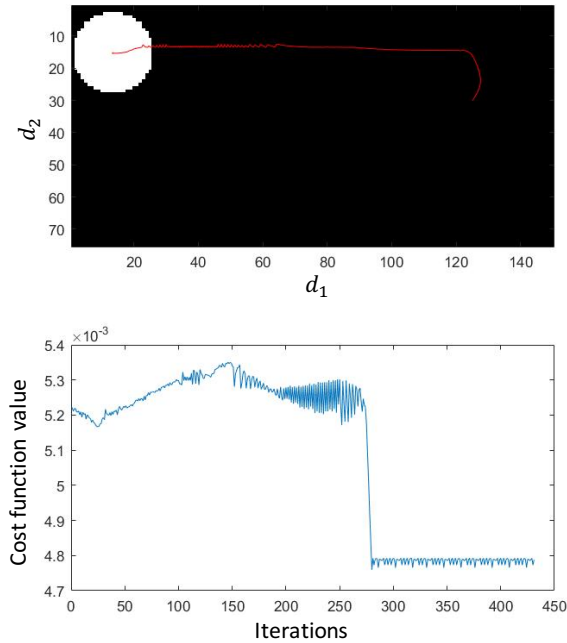


Figure B.24: Optimization results for the location of the hole from an initial position: trajectory of the center (top, in red) and value of the cost function (bottom) along the iterations.

682 We observe that there is a clear convergence to a local minimum in a rapid and effective  
 683 manner. Oscillations which can be observed in the value of the cost function are purely due  
 684 to geometrical reasons. Indeed, the hole is defined from pixels which induces that the shape  
 685 of the hole surface numerically evolves during the iterations.

686 [1] G. Allaire, *Shape optimization by the homogenization method*. Springer-Verlag, New-York 2002.  
 687 [2] G. Allaire, *Conception optimale des structures*. Springer, New-York 2002.  
 688 [3] G. Allaire, F. Jouve, A.M. Toader, Structural optimization using sensitivity analysis and a level-set  
 689 method. *Journal for Computational Physics* 2004; **194(1)**:363–393.  
 690 [4] G. Allaire, C. Dapogny, A. Faure, G. Michailidis, Shape optimization of a layer by layer mechanical  
 691 constraint for additive manufacturing. *Comptes Rendus de l'Académie des Sciences, Mathématique*  
 692 2017; **355(6)**:699–717.  
 693 [5] G. Allaire, C. Dapogny, R. Estevez, A. Faure, G. Michailidis, Structural optimization under overhang  
 694 constraints imposed by additive manufacturing technologies. *Journal of Computational Physics* 2017;  
 695 **351**:295–328.  
 696 [6] G. Andrade-Campos, J.A. Oliveira, *Engineering Optimization Workshop, Aveiro, Portugal* 2013.

- 697 [7] E. Andreassen, A. Clausen, M. Schevenels, B.S. Lazarov, O. Sigmund, Efficient topology optimization  
698 in Matlab using 88 lines of code. *Structural and Multidisciplinary Optimization* 2011; **43(1)**:1–16.
- 699 [8] S. Avril, F. Pierron, General framework for the identification of constitutive parameters from full-field  
700 measurements in linear elasticity. *International Journal of Solids and Structures* 2007; **44(14-15)**:4978–  
701 5002.
- 702 [9] S. Avril, M. Bonnet, A.S. Bretelle, M. Grediac, F. Hild, P. Ienny, F. Latourte, D. Lemosse, S. Pagano, E.  
703 Pagnacco, F. Pierron, Overview of identification methods of mechanical parameters based on full-field  
704 measurements. *Experimental Mechanics* 2008; **48(4)**:381–402.
- 705 [10] B.K. Bay, T.S. Smith, D.P. Fyhrie, M. Saad, Digital volume correlation: three-dimensional strain  
706 mapping using X-ray tomography. *Experimental Mechanics* 1999; **39(3)**:217–226.
- 707 [11] M. Ben Azzouna, J.N. Périé, J.M. Guimard, F. Hild, S. Roux, On the identification and validation of an  
708 anisotropic damage model using full-field measurements. *International Journal of Damage Mechanics*  
709 2011; **20**:1130–1150.
- 710 [12] M.P. Bendsoe, N. Kikuchi, Generating optimal topologies in structural design using a homogenization  
711 method. *Computer Methods in Applied Mechanics and Engineering* 1988; **71**:197–224.
- 712 [13] M.P. Bendsoe, Optimal shape design as a material distribution problem. *Structural Optimization* 1989;  
713 **1**:193–202.
- 714 [14] M.P. Bendsoe, O. Sigmund, *Topology optimization: theory, methods and applications*. Springer-Verlag,  
715 Berlin Heidelberg 2003.
- 716 [15] M. Bertin, F. Hild, S. Roux, Optimization of a cruciform geometry for the identification of constitutive  
717 parameters based upon full-field measurements. *Strain* 2016; **52**:307–323.
- 718 [16] G. Besnard, F. Hild, S. Roux, “Finite-element” displacement fields analysis from digital images: ap-  
719 plication to Portevin-Le Châtelier bands. *Experimental Mechanics* 2006; **46(6)**:789–803.
- 720 [17] B. Bourdin, Filters in topology optimization. *International Journal for Numerical Methods in Engi-  
721 neering* 2001; **50**:2143–2158.
- 722 [18] B. Bourdin, A. Chambolle, The phase-field method in optimal design. *IUTAM Symposium on Topo-  
723 logical Design Optimization of Structures, Machines and Materials* 2006; **137**:207–215.
- 724 [19] A. Bouterf, S. Roux, F. Hild, G. Vivier, X. Brajer, E. Maire, S. Meille, Damage law identification from  
725 full field displacement measurement: application to four-point bending test for plasterboard. *European  
726 Journal of Mechanics A/Solids* 2015; **49**:60–66.
- 727 [20] T.E. Bruns, A reevaluation of the SIMP method with filtering and an alternative formulation for  
728 solid-void topology optimization. *Structural and Multidisciplinary Optimization* 2005; **30(6)**:428–436.
- 729 [21] A. Buljac, C. Jailin, A. Mendoza, J. Neggers, T. Taillandier-Thomas, A. Bouterf, B. Smaniotto, F.  
730 Hild, S. Roux, Digital volume correlation: review of progress and challenges. *Experimental Mechanics*

- 731 2018; **58(5)**:661–708.
- 732 [22] M. Burger, S.J. Osher, A survey on level set methods for inverse problems and optimal design. *European*  
733 *Journal of Applied Mathematics* 2005; **16(2)**:263–301.
- 734 [23] A. Catapano, B. Desmorat, P. Vannucci, Stiffness and strength optimization of the anisotropy distribu-  
735 tion for laminated structures. *Journal of Optimization Theory and Applications* 2015; **167(1)**:118–146.
- 736 [24] D. Claire, F. Hild, S. Roux, Identification of a damage law by using full-field displacement measure-  
737 ments. *International Journal of Damage Mechanics* 2007; **16(2)**:179–197.
- 738 [25] B. Desmorat, G. Duvaut, Compliance optimization with nonlinear elastic materials: application to  
739 constitutive laws dissymmetric in tension-compression. *European Journal of Mechanics, A/Solids* 2003;  
740 **22**:179–192.
- 741 [26] B. Desmorat, Structural rigidity optimization with an initial design dependent stress field: application  
742 to thermo-elastic stress loads. *European Journal of Mechanics, A/Solids* 2013; **37**:150–159.
- 743 [27] B. Desmorat, Structural rigidity optimization with frictionless unilateral contact. *International Journal*  
744 *of Solids and Structures* 2007; **44**:1132–1144.
- 745 [28] N. Feld, H. Laeuffer, S. Roux, Constitutive identification of laminated composite materials using  
746 heterogeneous full field measurement. *Comptes-Rendus des JNC 19* 2015.
- 747 [29] M.B. Fuchs, S. Jiny, N. Peleg, The SRV constraint for 0/1 topological design. *Structural and Multidis-*  
748 *ciplinary Optimization* 2005; **30(4)**:320–326.
- 749 [30] D. Garcia, J.J. Orteu, L. Penazzi, A combined temporal tracking and stereo-correlation technique for  
750 accurate measurement of 3D displacements: application to sheet metal forming. *Journal of Materials*  
751 *Processing Technology* 2002; **125-126**:736–742.
- 752 [31] R. Gras, H. Leclerc, F. Hild, S. Roux, J. Schneider, Identification of a set of macroscopic elastic  
753 parameters in a 3D woven composite: uncertainty analysis and regularization. *International Journal*  
754 *of Solids and Structures* 2015; **55**:2–16.
- 755 [32] A. Gersborg-Hansen, M.P. Bendsoe, O. Sigmund, Topology optimization of heat conduction problems  
756 using the finite volume method. *Structural and Multidisciplinary Optimization* 2006; **31(4)**:251–259.
- 757 [33] M. Grédiac, F. Hild (ed), *Full-field measurements and identification in solid mechanics*. Wiley, New  
758 York 2013.
- 759 [34] F. Hild, S. Roux, Digital image correlation: from displacement measurement to identification of elastic  
760 properties - a review. *Strain* 2006; **42(2)**:69–80.
- 761 [35] F. Hild, S. Roux, CORRELI Q4: a software for “finite-element” displacement field measurements by  
762 digital image correlation. *Internal Report, LMT* 2008; **269**.
- 763 [36] F. Hild, S. Roux, Digital image correlation. in *Optical Methods for Solid Mechanics: A Full-Field*  
764 *Approach*, P. Rastogi and E. Hack eds., Wiley-VCH, Weinheim 2012; 183–228.

- 765 [37] F. Hild, S. Roux, Comparison of local and global approaches to digital image correlation. *Experimental*  
766 *Mechanics* 2012; **52(9)**:1503–1519.
- 767 [38] F. Hild, A. Bouterf, L. Chamoin, H. Leclerc, F. Mathieu, J. Neggers, F. Pled, Z. Tomicevic, S. Roux,  
768 Toward 4D mechanical correlation. *Advanced Modeling and Simulation in Engineering Sciences* 2016;  
769 **3**:17.
- 770 [39] C. Jailin, A. Carpiuc, K. Kazymyrenko, M. Poncelet, H. Leclerc, F. Hild, S. Roux, Virtual hybrid test  
771 control of sinuous crack. *Journal of the Mechanics and Physics of Solids* 2017; **102**:239-256.
- 772 [40] K.T. Kavanagh, R.W. Clough, Finite element applications in the characterization of elastic solids.  
773 *International Journal of Solids and Structures* 1971; **7**:11–23.
- 774 [41] U.D. Larsen, O. Sigmund, S. Bouwstra, Design and fabrication of compliant micromechanisms and  
775 structures with negative Poisson’s ratio. *Journal of Microelectromechanical systems* 1997; **6(2)**:99–106.
- 776 [42] F. Latourte, A. Chrysochoos, S. Pagano, B. Wattrisse, Elastoplastic behavior identification for hetero-  
777 geneous loadings and materials. *Experimental Mechanics* 2008; **48**:435–449.
- 778 [43] H. Leclerc, J-N. Périé, S. Roux, F. Hild, Integrated digital image correlation for the identification of  
779 mechanical properties. *MIRAGE 2009, Lecture Notes in Computer Science* 2009; **5496**:161–171.
- 780 [44] H. Leclerc, J. Neggers, F. Mathieu, F. Hild, S. Roux, Correli 3.0.  
781 *IDDN.FR.001.520008.000.S.P.2015.000.31500*, Agence pour la Protection des Programmes, Paris  
782 2015.
- 783 [45] D. Lecompte, A. Smits, H. Sol, J. Vantomme, D. Van Hemelrijck, Mixed numerical-experimental  
784 technique for orthotropic parameter identification using biaxial tensile test on cruciform specimens.  
785 *International Journal of Solids and Structures* 2007; **44**:1643–1656.
- 786 [46] K. Levenberg, A method for the solution of certain nonlinear problems in least squares. *Quarterly of*  
787 *Applied Mathematics* 1944; **2(2)**:164–168.
- 788 [47] F. Mathieu, H. Leclerc, F. Hild, S. Roux, Estimation of elastoplastic parameters via weighted FEMU  
789 and integrated-DIC. *Experimental Mechanics* 2015; **55**:105–119.
- 790 [48] N. McCormick, J. Lord, Digital image correlation. *Materials today* 2010; **13(12)**:52–54.
- 791 [49] J. Molimard, R. Le Riche, A. vautre, J.R. Lee, Identification of the four orthotropic plate stiffnesses  
792 using a single open-hole tensile test. *Experimental Mechanics* 2005; **45**:404–411.
- 793 [50] J. Neggers, F. Mathieu, F. Hild, S. Roux, N. Swiergiel, Improving full-field identification using pro-  
794 gressive model enrichments. *International Journal of Solids and Structures* 2017; **118-119**:213–223.
- 795 [51] J. Neggers, O. Allix, F. Hild, S. Roux, Big data in experimental mechanics and model order reduction:  
796 today’s challenges and tomorrow’s opportunities. *Archives of Computational Methods in Engineering*  
797 2018; **25(1)**:143–164.
- 798 [52] J.A. Norato, M.P. Bendsoe, R.B. Haber, D.A. Tortorelli, A topological derivative method for topology

- 799 optimization. *Structural and Multidisciplinary Optimization* 2007; **33(4)**:375–386.
- 800 [53] F. Palacios-Gomez, L. Lasdon, M. Engquist, Nonlinear optimization by successive linear programming.  
801 *Management Science* 1982; **28**:1106–1120.
- 802 [54] J.C. Passieux, F. Bugarin, C. David, J.N. Périé, L. Robert, Multiscale displacement field measurement  
803 using digital image correlation: application to the identification of elastic properties. *Experimental*  
804 *Mechanics* 2015; **55**:121–137.
- 805 [55] J.M. Pérez Zerpa, G.D. Maso Talou, P.J. Blanco, A new robust formulation for optical-flow/material  
806 identification problems. *Computer Methods in Applied Mechanics and Engineering* 2019; **351**:766–788.
- 807 [56] T. Pottier, P. Vacher, F. Toussaint, H. Louche, T. Coudert, Out-of-plane testing procedure for inverse  
808 identification purpose: application in sheet metal plasticity. *Experimental Mechanics* 2012; **52(7)**:951–  
809 963.
- 810 [57] N. Ranaivomiarana, F.X. Irisarri, D. Bettebghor, B. Desmorat, Concurrent optimization of material  
811 spatial distribution and material anisotropy repartition for two-dimensional structures. *Continuum*  
812 *Mechanics and Thermodynamics* 2019; **31(1)**:133–146.
- 813 [58] J. Réthoré, S. Roux, F. Hild, Noise-robust stress intensity factor determination from kinematic field  
814 measurements. *Engineering Fracture Mechanics* 2006; **75(13)**:3763–3781.
- 815 [59] J. Réthoré, F. Hild, S. Roux, Extended digital image correlation with crack shape optimization.  
816 *International Journal for Numerical Methods in Engineering* 2007; **73(2)**:248–272.
- 817 [60] J. Réthoré, F. Hild, S. Roux, An extended and integrated digital image correlation technique applied  
818 to the analysis of fractured samples. *European Journal of Computational Mechanics* 2009; **18**:285–306.
- 819 [61] J. Réthoré, Muhibullah, T. Elguedj, M. Coret, P. Chaudet, A. Combescure, Robust identification  
820 of elasto-plastic constitutive law parameters from digital images using 3D kinematics. *International*  
821 *Journal of Solids and Structures* 2013; **50(1)**:73–85.
- 822 [62] S. Roux, F. Hild, Stress intensity factor measurements from digital image correlation: post-processing  
823 and integrated approaches. *International Journal of Fracture* 2006; **140(1–4)**:141–157.
- 824 [63] S. Roux, F. Hild, Digital image mechanical identification (DIMI). *Experimental Mechanics* 2008;  
825 **48(4)**:495–508.
- 826 [64] S. Roux, F. Hild, Optimal procedure for the identification of constitutive parameters from experimen-  
827 tally measured displacement fields. *International Journal of Solids and Structures* 2018; in press.
- 828 [65] O. Sigmund, A 99 line topology optimization code written in Matlab. *Structural and Multidisciplinary*  
829 *Optimization* 2001; **21**:120–127.
- 830 [66] O. Sigmund, K. Maute, Topology optimization approaches: a comparative review. *Structural and*  
831 *Multidisciplinary Optimization* 2013; **48(6)**:1031–1055.
- 832 [67] S.N. Sorensen, E. Lund, Topology and thickness optimization of laminated composites including man-

- 833       ufacturing constraints. *Structural and Multidisciplinary Optimization* 2013; **48(2)**:249–265.
- 834 [68] M. Stolpe, K. Svanberg, An alternative interpolation scheme for minimum compliance topology opti-  
835       mization. *Structural and Multidisciplinary Optimization* 2001; **22(2)**:116–124.
- 836 [69] M. Sutton, W. Wolters, W. Peters, W. Ranson, S. McNeill, Determination of displacements using an  
837       improved digital correlation method. *Image Vision Computing* 1983; **1(3)**:133–139.
- 838 [70] M.A. Sutton, F. Hild, Recent advances and perspectives in digital image correlation. *Experimental*  
839       *Mechanics* 2015; **55(1)**:1–8.
- 840 [71] K. Svanberg, The method of moving asymptotes - a new method for structural optimization. *Interna-*  
841       *tional Journal for Numerical Methods in Engineering* 1987; **24**:359–373.
- 842 [72] C.C. Swan, I. Kosaka, Voigt-Reuss topology optimization for structures with linear elastic material  
843       behaviours. *International Journal for Numerical Methods in Engineering* 1997; **40**:3033–3057.